MULTIWAVELENGTH SELECTION OF OBSCURED AGN

AND CONTRIBUTIONS TO THE X-RAY BACKGROUND

by

BRANYON MANNING MAY

WILLIAM C. KEEL, COMMITTEE CHAIR
GENE G. BYRD
D. MICHAEL CRENSHAW
JIMMY A. IRWIN
PIETER B. VISSCHER
RAYMOND E. WHITE

A DISSERTATION

Submitted in partial fulfillment of the requirements
for the degree of Doctor of Philosophy
in the Department of Physics and Astronomy
in the Graduate School of
The University of Alabama

TUSCALOOSA, ALABAMA

2011

Copyright Branyon Manning May 2011
ALL RIGHTS RESERVED

ABSTRACT

Obscuration in AGN is a crucial component to understanding the observed spectrum of the X-ray Background. We tested numerous AGN selection techniques in X-ray, mid-infrared, and optical to test for multiwavelength correlations and to help establish selection criteria for obscured AGN. With AGN sources dominating background X-ray sources, we selected medium-depth archival Chandra observations covering 5.6 deg^2 of sky and generating a large sample of serendipitous X-ray sources (>10,000). The mid-infrared component came from archival *Spitzer* data, with ~3,500 sources being detected in at least two IRAC bands and 1,485 in all 4 bands. For the optical component, greater than 70% of the Chandra observations also had full coverage within the SDSS Data Release 7, yielding > 2,300 optical counterparts and 125 spectra. In analyzing the sample, we have identified the parameter spaces in the X-ray/mid-infrared/optical that are optimized for containing members of the elusive class of obscured AGN, and provide a candidate list. We cross-check our X-ray number counts and source densities with contributions to the X-ray background, and find that we resolve approximately 90% of the X-ray Background in the 0.5-8.0 keV range. Testing populations divided on X-ray hardness and flux-level confirms that the unresolved hard X-ray background will be dominated by large populations of increasingly fainter and harder sources.

DEDICATION

I dedicate this work to all my family and friends who encouraged me over these many years. The most obvious support was found in my wife and kids whose patience was enduring, and in my family and church family who at various stages supplied where I lacked.

LIST OF ABBREVIATIONS AND SYMBOLS

AGN	Active Galactic Nucleus
BLAGN	Broad Line Active Galactic Nucleus
f, F	Flux
HR	Hardness Ratio
IR	Infrared
keV	Kiloelectron Volt
L	Luminosity
Mrk	Markarian galaxy catalogue
$M_{\odot}$	Solar Mass
N_{H}	Neutral Hydrogen Column Density
NLAGN	Narrow Line Active Galactic Nucleus
PL	Power-law
QSO	Quasi-Stellar Object
Sy	Seyfert galaxy
u', g', r', i', z'	Sloan Digitized Sky Survey filters
ULX	Ultraluminous X-ray Source
XRB	X-ray Background
z	Redshift
α	Spectral Index

Γ	Photon Index
υ	Frequency
σ	Standard Deviation
σ_T	Thompson Cross-section

ACKNOWLEDGMENTS

I have been afforded great blessings throughout my life, radiant as the stars in the heavens—without number. Yet from my human perspective several blessings shine as the brightest of stars, having enabled me to navigate the roughest of seas. My wife, Alana, is one of these shining stars—loving, strong, encouraging, and faithful. God knew my many deficiencies and through Alana has supplied their answer. She also has given unselfishly of herself as a wife and a loving mother to our beautiful children, Branna Rose and Atlie Claire, two more stars in my life, who came with great joy and many prayers. Of course, I owe enormous gratitude to my parents, Larry and Janis, for the preparation and guidance as I traversed such a journey, and to my sister, Kristen, and brother, Cameron, who trained and grew with me in the unique bonds that siblings have. Many others, including extended family, close friends, and the family in the Lord's Church constitute the constellations of blessings that fill my sky.

For this project, I was aided by my advisor, Bill Keel, whose office across the hall from mine was always open. Several others within the department and without provided technical help, along with funding along the way through the NASA Graduate Student Researchers Program (GSRP).

CONTENTS

ABSTRACT ii

DEDICATION iii

LIST OF ABBREVIATIONS AND SYMBOLS iv

ACKNOWLEDGMENTS vi

LIST OF TABLES x

LIST OF FIGURES xi

1. INTRODUCTION 1

A. Active Galactic Nuclei 1

B. The X-ray Background 2

C. Project Strategy 5

2. SURVEY SELECTION 11

A. X-ray Field Selection 11

B. X-ray Processing 14

i. Data Screening and Reprocessing 15

ii. Source Detection and Extraction 16

iii. Detection Probability Rate 19

iv. Positional Error and Usable FOV 22

v. X-ray Source Catalog 24

C. Multiwavelength Source Correlations 24

i. Mid-Infrared Spitzer Correlations 24

ii. Optical SDSS Correlations 26

iii. Spectroscopic Correlations 27

D. Mid-Infrared Versus Optical Correlations 28

3. X-RAY PROPERTIES 30

A. Photometric Properties 30

i. Hardness Ratio 30

ii. Source Flux Determination 32

B. X-ray Spectral Fitting 34

4. MULTIWAVELENGTH SOURCE PROPERTIES 40

A. Spitzer IRAC Mid-Infrared Characterization 40

i. Mid-Infrared AGN Source Properties 40

ii. Mid-Infrared AGN Selection: Infrared Power-law Selection 40

iii. Mid-Infrared AGN Selection: Color-Space "Wedge" Technique 43

B. Optical Source Properties 47

i. Optical AGN Selection: Optical Power-law Selection 48

ii. Optical AGN Selection: X-ray-to-Optical Flux Ratio 49

C. Optical-Infrared AGN Selection: The α_{Opt}–α_{IR} Relation 52

D. Optical-Infrared AGN Selection: IRAC-SDSS Color Wedge 54

E. Candidate Obscured AGN 56

F. ULX & X-ray Binary Candidates Contaminating the AGN Sample56

5. X-RAY BACKGROUND 58

A. X-ray Number Counts 58

B. Unresolved and Resolved XRB Fractions.....61

i. Estimation to the X-ray Background Peak.....63

6. CONCLUSION.....65

A. Summary 65

B. Concluding Remarks.....67

REFERENCES 69

LIST OF TABLES

Table 1: X-ray Energy Bands 75

Table 2: X-ray Survey Comparisons 75

Table 3: X-ray Observations 76

Table 4: Mid-Infrared Source Statistics 80

Table 5: Candidate Obscured AGN 81

Table 6: XRB Intensities 83

LIST OF FIGURES

Figure 1. The X-ray Background Spectrum.....3

Figure 2. Unified Model of AGN 5

Figure 3. Effect of Varying the Column Density.....9

Figure 4: Exposure Length Distribution 12

Figure 5: X-ray Surveys.....14

Figure 6: Example of the WAVDETECT Output 18

Figure 7: MARX Source Detection Simulation 21

Figure 8: Detection Rate versus Off-Axis Angle 21

Figure 9: PSF Growth Versus Off-Axis Angle.....23

Figure 10: Positional Uncertainty Versus Off-Axis Angle 23

Figure 11: Example of Chandra and Spitzer FOVs 25

Figure 12: Redshift distributions. 28

Figure 13: Spectroscopic Versus Photometric Redshifts 29

Figure 14: HR Distribution. 31

Figure 15: Photon Index Distribution for Spectral Sample 36

Figure 16: Effects of Absorption on Hardness Ratio.....38

Figure 17: Redshift Effect on the Hardness Ratio and Column Density...39

Figure 18: Distribution of Mid-Infrared Power-Law Slopes. 42

Figure 19: Mid-Infrared AGN Selection Criteria by Stern et al.....44

Figure 20: Mid-Infrared AGN "Wedge" Selection by Lacy et al. 46

Figure 21. X-ray Column Density Distribution in Stern IR color space ...47

Figure 22: Optical Power Law Distributions 49

Figure 23: Optical Magnitude versus X-ray Flux 50

Figure 24: X-ray-to-Optical Flux Ratio versus Hard X-ray Luminosity...51

Figure 25: SED Templates of AGN, Starburst, and Normal Galaxy Types52

Figure 26: Optical Power-law versus Mid-Infrared Power-law.....54

Figure 27: SDSS *z*' - IRAC Color Wedge 55

Figure 28: SDSS *i*'-IRAC Color Wedge 56

Figure 29: ACIS Observation Sensitivity Map 58

Figure 30: Effective Area Curve 59

Figure 31: log*N*-log*S* distribution.....60

1. INTRODUCTION

Current understanding attributes much of the observed radiation in the universe to accretion processes, especially in very distant sources. To efficiently generate the amount of observed energy, the process of mass accretion is proposed to occur around black holes (defined as extremely massive, compact objects). On the scale of a galaxy, the total energy production is thought to be dominated by a supermassive black hole ($M_{\bullet} > 10^6 M_{\odot}$). Although black holes are thought to exist in practically every galaxy, Active Galactic Nuclei (AGNs) are an obvious set of candidates for studying accretion processes.

A. Active Galactic Nuclei

A diversity of AGN classes exists, accommodating both the contrasting spectral features and luminosities in their spectral energy distributions. Under unification scenarios, the AGN varieties are explained through various orientation effects relating to the line-of-sight between observer and central accretion source. A broad division based on the optical is made between unobscured (type-1) and obscured (type-2) sources. Analogous to this optical dichotomy, a division based on X-ray emission also is made separating unabsorbed and absorbed sources. Historically, the optically unobscured and the X-ray unabsorbed AGN were identified first in their respective regimes due to the fact that their nuclear emission was a substantial portion of the galaxy's emission. The spectral signatures also were distinct from their host galaxy contributions. Optically obscured and X-ray absorbed AGN, on the other hand, were postulated based on both unification scenarios and X-ray background modeling. These AGN should consist

of equally powerful accretion onto supermassive black holes, yet will have large amounts of gas and dust blocking the line-of-sight to the central region of activity.

B. The X-ray Background

For almost 50 years, astronomers have been seeking to further understand the X-ray background (XRB). In 1962, Giacconi, Gursky, Paolini, and Rossi serendipitously discovered a direction-independent X-ray signal using a rocket-born experiment intended to study the Moon's X-ray signature. Although lunar X-rays were not detected, the discovery of the XRB and the first X-ray source outside the solar system, Scorpius (Sco) X-1, were invaluable achievements. Ironically in 1991, Schmitt et al. showed how observations of the Moon in X-rays, made by the Röntgen satellite (ROSAT), revealed the cosmic origin (at least extra-solar) of the XRB. This result was demonstrated by showing the Moon's dark side was fainter than the surrounding background levels of the field-of-view. In the late 1970s, the High Energy Astrophysics Observatory (HEAO-1) satellite made early spectral measurements of the XRB, which was found to peak around 30 keV (see Figure 1) with the lower energies being fit very well by a simple power-law, having an index to the photon spectrum ~1.4 (Marshall et al., 1980).

A diffuse intergalactic medium (IGM) was proposed, at first, as the most likely origin for the XRB (Cowsik & Kobetich, 1972; Field & Perrenod, 1977), whereas the contributions from discrete sources, though acknowledged, were given less significance. However, by the mid-1980s, the individual source contributions (especially of Active Galactic Nuclei—AGN) began to be given greater significance (Schmidt & Green, 1986). As the available AGN X-ray spectra were increasing in number, their global contributions could be removed from the overall XRB, which left a residual energy spectrum that was too flat and required higher energy X-rays than

the hypothesized IGM models. In their review article, Fabian and Barcons (1992) discussed the incompatibilities of the XRB coming from the emission of an optically-thin medium (i.e., the IGM), and stated that the simplest interpretation of the data was that the XRB was due to a "new" class of sources. This conclusion agrees well with what they summarized about the current state of X-ray astronomy, which they characterized in the Introduction as currently lacking enough angular resolution and sensitivity to identify all of the XRB sources.

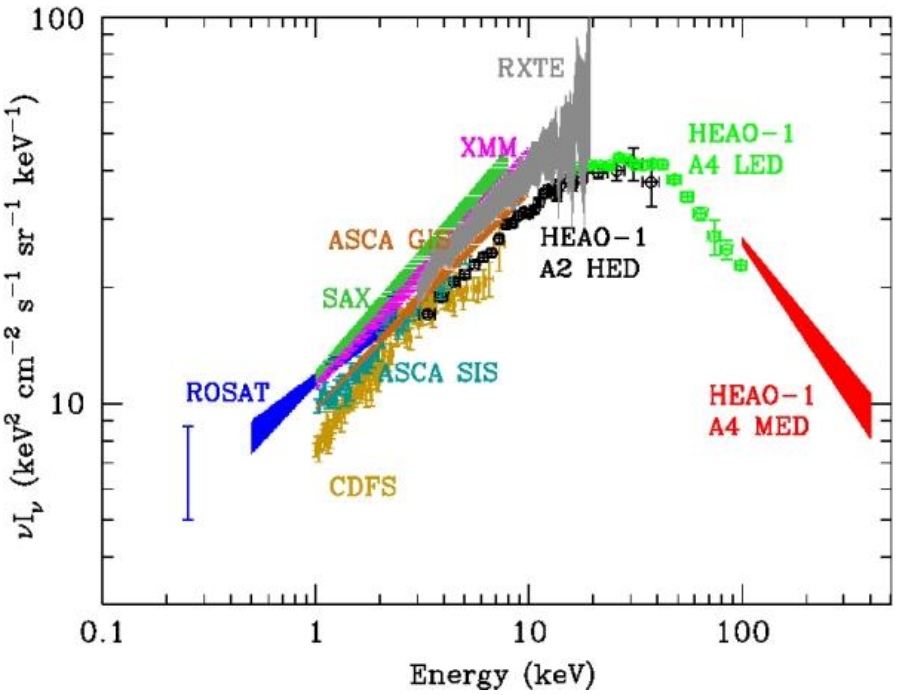

Figure 1. The X-ray Background Spectrum
The figure shows the spectrum of the X-ray background, as measured by numerous satellites over the years. The peak roll-over is at ~30 keV, which is a much harder energy than the average unobscured AGN peaks, thus implying the existence of another class of source with large contributions at increasing energy. This figure comes from the Cambridge University Astronomy website (www-xray.ast.cam.ac.uk).

In recent years, the XRB has fallen under more intense scrutiny because the astounding achievements of NASA's Chandra X-ray Observatory (CXO), which increased detection sensitivity by 20 fold and spatial resolution some eight fold over any previous mission. Today much effort is being made to resolve the XRB into discrete source contributions, which has been

more successful at energies below 6 keV, while less complete at the higher energies (Caccianiga et al., 2004; Treister & Urry, 2005). Worsley et al. (2006) stated that only ~60% of the XRB has been resolved in the 6-8keV range, and ~50% at energies > 8 keV. Most of the discrete sources have been identified as AGN. However, the peak of the XRB spectrum is at a much higher energy than seen in the spectrum of the first, historically-identified class of AGN, which typically have a photon index of ~1.7 (Fabian & Barcons, 1992; Marshall et al., 1980). This spectrum declines more steeply from the lower energy ("soft") X-rays down through the higher energy ("hard") X-rays, than the spectrum of the XRB. Due to this discrepancy between the hard (higher energy) peak of the XRB and the soft (lower energy) peak of the known AGN, observations were sought to determine the dominant, discrete source producing such an effect. Ensuing observations have shown a class of highly obscured AGN, which have their soft X-ray component almost entirely absorbed by some enshrouding material, leaving a dominant hard X-ray component. This more recently discovered class of AGN offers a very real solution for the hardness problem of the XRB. Subsequently, XRB-AGN models have been developed in an effort to account for these two general types of observed AGN—that is, the unobscured, soft X-ray excess (type-1) AGN and the obscured, hard X-ray excess (type-2) AGN. These XRB synthesis models endeavor to explain the observed spectrum through various mixtures of obscured and unobscured, based on the unified scheme, which is illustrated in Figure 2 (c.f., Antonucci, 1993; Urry & Padovani, 1995; Brandt & Hasinger, 2005; Nenkova, Sirocky, Nikutta, Ivezić, & Elitzur, 2008). Previous seminal works by Comastri et al. (1995, 2001), Gilli et al. (2001, 2007), and Ueda et al. (2003) outlined a framework within the standard AGN-model by which the XRB could possibly be reproduced. Each of these works built on the observational

constraints available in order to match AGN population estimates to theoretical contributions in the XRB. In filling a niche between past surveys, such as the shallow ROSAT All-Sky Survey (RASS) and the deep, pencil-beam Chandra Deep Fields (CDF-North and -South), we are seeking to further the observational constraints on the standard AGN-model from which the XRB contributions can be correlated more precisely.

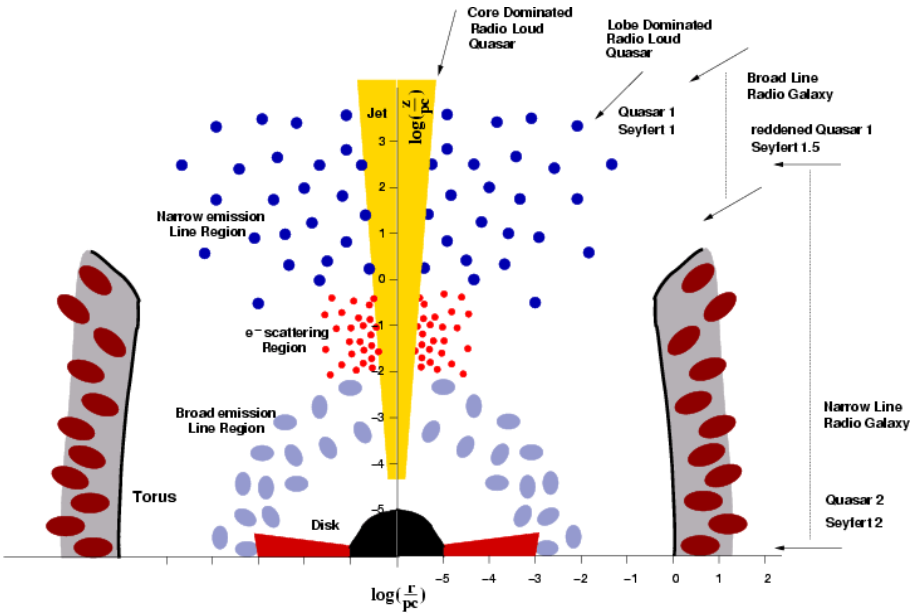

Figure 2. Unified Model of AGN
This figure demonstrates the theoretical model of AGN unification, where the observed differences are due primarily to the various orientations of viewing angle. This figure comes from Zier & Biermann (2002).

C. Project Strategy

Following two lines of evidence for the existence of obscured AGN: (1) the implications of the unified scenario and (2) constraints from XRB analysis, we can discuss how many obscured AGN might exist. The number of obscured AGN, or rather the ratio of obscured to unobscured, is important in understanding the cosmic energy budget and investigating the interplay between galaxy hosts and their supermassive black holes.

In testing the standard unification model, there are numerous questions that are in need of addressing. Though AGN commonly are discussed with a clear distinction between types, the demarcation between these types is not quite as clear. Multiwavelength analyses of AGN across the type-spectrum, with more intense scrutiny on those falling between the standard types, will help to clarify the physical differences that are producing the observational distinctions.

The traditionally accessible surveys in optical and soft X-ray ($E < 2$ keV) are severely biased toward type-1 (unobscured) AGN where host light is dominated by the nucleus. Two pass bands that minimize the biases for obscuration in AGN are the hard (2-10 keV) X-ray and mid-infrared. These complementary bands expose both the direct emission as X-rays from the central engine (proposed accretion from the supermassive black hole) and the mid-infrared emission (rest-frame $\lambda \sim 2\mu m$) dominated by emission from the dusty obscuring material (Krolik, 1999; Eckart et al., 2010). Though these bands minimize biases, they still suffer from incomplete selection. For example, fractions of X-ray selected and mid-IR selected AGN go undetected (or at least unidentified by selection methods) in observations of the other range. Similarly, between X-ray selected and optically selected AGN there are fractions of non-detections when viewing the opposite band. Steidel et al. (2002) describe optically selected AGN that are undetected in deep X-rays, while Comastri et al. (2002) describes so called XBONGs (X-ray Bright Optically Normal Galaxies) selected in X-rays but unidentified in optical spectra.

In view of the above problems, we compiled a moderate-depth X-ray based sample for this project, with greater than 5.6 deg^2 of sky coverage. Using this sample, we began a search for non-targeted (serendipitous) AGN within the fields of the selected, archived observations. Lists of candidate sources were generated, using a tailored data reduction pipeline described below in

Section 2.B Within the candidate lists, the majority of the sources do not have the number of counts necessary to be considered spectral-quality, yet are of great use statistically for their positional data, fluxes, hardness ratios, and column density (N_H) estimation. The ability to gather spectral-quality data is governed by the exposure length and observed luminosities of the sources. Thus as we discussed, the sample parameters were chosen in order to maximize the effectiveness of such a survey.

As their name suggests, active galaxies show activity through their X-ray signature, which is thought to yield distinctions in their flux ratios, X-ray-to-infrared (f_x/f_{ir}) and X-ray-to-optical (f_x/f_o) from normal, inactive galaxies. Combining the X-ray with infrared and optical data, relationships among the X-ray selected candidates are examined based on the photometric properties. AGN have also been found to occupy particular regions of IR color-space (de Grijp, Miley, Lub, & de Jong, 1985). Using techniques that have been employed previously with both 2MASS (Leipski et al., 2005) and Spitzer (Lacy et al., 2004; Stern et al., 2005) data, we performed analyses of IR colors to test X-ray and IR relationships for our source candidates. Making use of the complementary aspects between the X-ray and infrared, Barmby et al. (2006) and Polletta et al. (2006) discussed the identification and determination of AGN, specifically highlighting the capabilities of Chandra and Spitzer. Further within the AGN sample, trends in IR emission relative to X-ray absorption help to characterize the state of the obscuring material.

Our project sought to constrain and extend results of prior surveys in this area of study. With that mindset, we sought to adopt, where applicable and beneficial, data conventions to enable appropriate comparisons between datasets. In the Chandra band pass, hard X-rays are those with energies greater than 2 keV, whereas soft X-rays are those below this threshold. This

convention is a natural result of the energy range covered by present X-ray telescopes, and is the similar convention adopted by other AGN surveys such as the Chandra Multiwavelength Project (ChaMP), the Serendipitous Extragalactic X-ray Source Identification (SEXSI) Project, and the Cosmic Evolution Survey (COSMOS). A common source analysis technique is to compare the source counts in differing energy bands, which for this survey are defined in Table 1. To facilitate an efficient analysis of these energy-bands, we employed a common technique known as the Hardness Ratio (HR) to compare counts within two energy bands, defined according to the previous Hard and Soft convention. Of course, this designation is a general form and the H and S can stand for any two energy ranges necessary, with the analysis remaining consistent as long as the H represents the upper of the two energy bands. For the determination of the source obscuration, a quantity known as the column density (N_H) will be used. The column density is a measurement that references the amount of absorption seen in the X-ray spectra. Again we followed standard values, which for the AGN types are: $N_H < 10^{22}$ cm^{-2} for type-1s, and $N_H > 10^{22}$ cm^{-2} for type-2s. Additionally, because the column density is related to the amount of obscuration, sources with $N_H > 10^{24}$ cm^{-2} are termed Compton-thick sources, because this corresponds to the inverse of the Thompson cross-section (σ_T). By $N_H \sim 10^{25}$ cm^{-2}, all X-ray energies below 10keV are obscured.

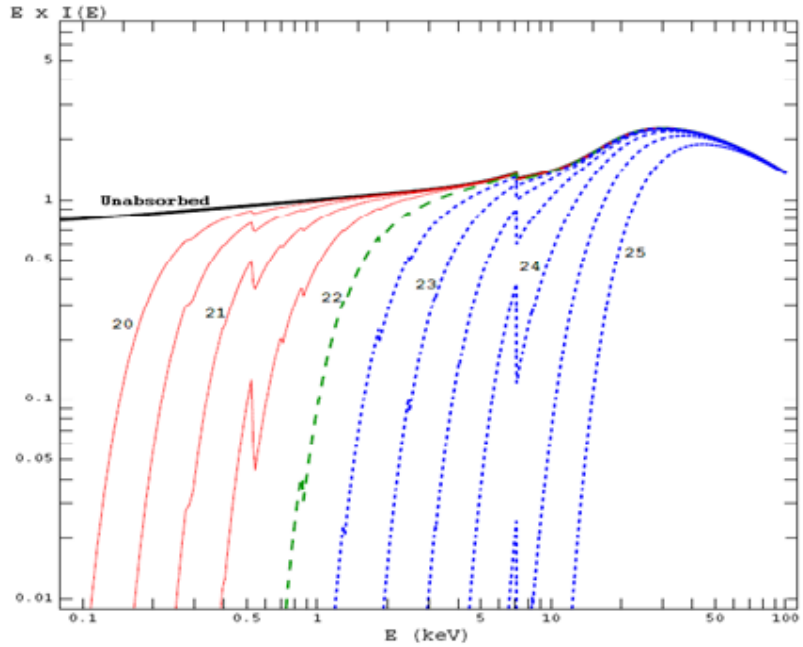

Figure 3. Effect of Varying the Column Density
This figure shows the effect of increasing the column density on a typical power-law model. The values next to the curves are log-values of the column density. The green dashed curve marks the usual transition between a relatively unobscured X-ray AGN to an obscured X-ray AGN.

There are two major contributions to the observed N_H: intrinsic and foreground. We will reduce the level of foreground absorption that is due to the Milky Way (on orders of ~10^{20}-10^{21} cm^{-2}) by setting constraints on our field selection (described in the following section), as well as accounting for the inherent residual effects that are in each field. This will leave the intrinsic absorption as the dominating factor, which is a key parameter in AGN X-ray classifications.

The structure of this paper is as follows. Section 2 presents the criteria used to select the serendipitous X-ray survey fields, the methodology for processing the X-ray data, and the data mining procedures for obtaining the multiwavelength correlations. Section 3 presents the X-ray photometric and spectral properties. Section 4 presents the multiwavelength AGN diagnostics applied to the sub-samples of X-ray detected AGN candidates. Section 5 presents the X-ray

number counts and contributions of the X-ray Background. Section 6 summarizes the conclusions of this X-ray, optical, and mid-infrared study, and includes final remarks.

2. SURVEY SELECTION

A. X-ray Field Selection

The sample selection phase of any project represents the most important, difficult, and possibly time-consuming hurdle. For the goals of this proposal, the sample is one that fills the niche between the past shallow, all-sky surveys and narrow-field deep surveys.

For the X-ray data, we limited ourselves to the data archive of NASA's Chandra mission, which has a much greater sensitivity and resolution than past missions, and has better angular resolution than the current XMM-Newton satellite operated by the European Space Agency (ESA). The selection criteria chosen for this project are different from those of the original observations. The following criteria were implemented for either inclusion or exclusion from the sample:

1. Inclusion of ACIS observations having a minimum exposure length of 60ks (between AO2-AO7). This minimum exposure length means that the flux (0.3-9.5keV) limited completeness for the AGN candidates, assuming $\Gamma = 1.7$, are ~9.0 x 10^{-16} ergs/cm^2/s and 7.54 x 10^{-16} ergs/cm^2/s for an unabsorbed source on the ACIS-I and -S arrays, respectively.[1] (The flux limits are derived assuming a minimum count rate of 8.33 x 10^{-5} counts/s, corresponding to a minimum detection limit of 5 counts in a 60ks exposure.)
2. Exclusion of observations within 20° of the galactic plane ($|b| \leq 20°$). This criterion was selected to minimize Galactic extinction and having our fields swamped with foreground Galactic targets. This latitude range corresponds to an $N_H < 6 \times 10^{20}$ cm^{-2} or an E(B-V) < 0.1 mag.

[1] See http://heasarc.gsfc.nasa.gov/Tools/w3pimms.html

3. Exclusion of observations that were part of previous deep surveys: CDF-North, CDF-South, and Lockman Hole.
4. Exclusion of observations pointed on large, extended targets such as the LMC, SMC, M31, M32, M33, M101, 47 Tuc, and NGC362.

Due to these criteria the resulting sample consists of 90 observations of 79 unique target fields chosen to provide X-ray coverage with a minimum exposure length of 60ks. Figure 4 shows the distribution of exposure lengths across this full sample. The average exposure length is approximately 81.1 ks, whereas the total exposure of all the observations is approximately 7.30 Ms. For the multiwavelength analysis, approximately 72% of our target field aim points (65 of 79) have partially overlapping mid-infrared observations in the Spitzer archive with the Infrared Array Camera (IRAC). For the additional optical component, approximately 56% of the target fields (51 of 79) have Sloan Digital Sky Survey (SDSS) photometric and spectroscopic coverage under Data Release 7.

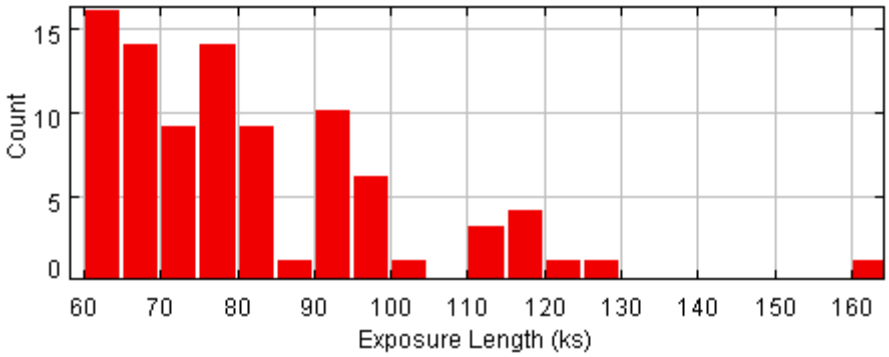

Figure 4: Exposure Length Distribution
The sample is comprised of 90 observations of 79 unique fields, where the exposure length distribution is relative to all, and does not sum over the overlapping fields. The average exposure length for this sample is approximately 81.1ks, whereas the total exposure of all the observations is approximately 7.30 Ms.

Of the Chandra observations in our survey, 78 had either five or six active chips with the total active chips summed for all observations equaling 449. Accounting for the 11 overlapping

observations, there were 386 active chips each approximately 8 arcminutes on a side, giving a total active field-of-view (FOV) of almost 7 square degrees. However, we need to introduce into our discussion the reduction of the usable field-of-view (FOV) due to the asymmetry and rapidly increasing point spread function (PSF) at large off-axis angles. The restrictions for the usable FOV are discussed below in Section 2.B.iv. Although the total coverage will be reduced, the extent of sky coverage will provide us with ~5.6 deg^2, offering the potential to generate large lists of serendipitous background sources (~10,000) from our X-ray sample, consisting primarily of AGN around the targeted objects. As was mentioned in the previous paragraph and is discussed further in Section 2.C.i, the Spitzer observations have only partial overlapping coverage. Thus for the 64 fields having Spitzer coverage, approximately 1.33 square degrees will have X-ray and two IRAC channels, and approximately 0.44 square degrees will have complete X-ray and IRAC coverage.

For comparison, Table 2 lists the statistical properties for several X-ray based multiwavelength surveys: the Calan-Yale Deep Extragalactic Research (CYDER) survey, the High Energy Large Area Survey (HELLAS2XMM), the Serendipitous Extragalactic X-ray Source Identification (SEXSI) project, and the Chandra Multiwavelength Project (ChaMP). Similarly Figure 5 shows the limiting flux and effective area parameter space for X-ray surveys spanning the range from the pencil-beam Chandra Deep Fields to the wide-area ROSAT NEP. These comparisons serve to illustrate that the depth and sky coverage of the current project matches well with other large area surveys and complements their coverage. Comparing overalp among other serendipitous surveys, there is only 1 SEXSI field and 6 ChaMP fields in our selected fields.

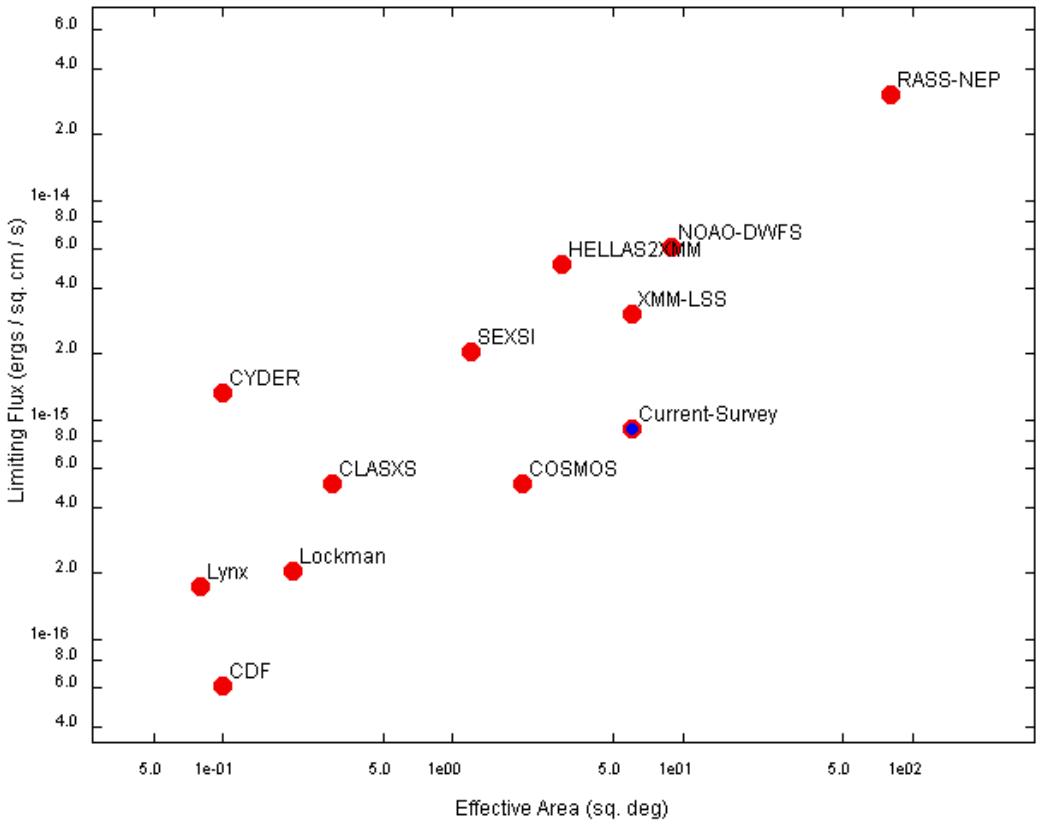

Figure 5: X-ray Surveys
X-ray surveys spanning the range of from the pencil beamChandra Deep Fields to the shallow wide-area RASS-NEP. The current survey is shown as a blue point, covering the medium depth, medium area space near the COSMOS survey.

B. X-ray Processing

With our sample defined and selected, we proceeded to develop a processing pipeline that would be tailored to provide the output needed for the specific goals of our project. For the data reduction portion of our pipeline, we used the standard Chandra processing software, CIAO[2], version 4.0 (3.4 for Sherpa routines). We made extensive use of the ability to script the CIAO processing routines, developing script-routines to process the Level-1 event files into new Level-2 event files, that would account for the most recent calibrations. The use of processing scripts also automated the tedious requirement of working with all chips (449) independently.

[2] http://asc.harvard.edu/ciao/

i. Data Screening and Reprocessing

For the X-ray data, we started with the Level-1 data products generated by the Chandra X-ray Center (CXC) standard data processing (SDP). These were used as the initial inputs to which we applied the calibration databases (CALDB v3.2.1). For all observations the SDP version was higher than DS-7.4.0 (for the FAINT datamode) or DS-7.6 (for the VFAINT datamode). With this verified, we used the command, acis_process_events, to process *new* Level-1 event files. This tool applies the gain map, the time-dependent gain correction, the charge transfer inefficiency (CTI) corrections, turns on/off pixel randomization, and applies an optional background cleaning to VFAINT mode observations. For this survey, the pixel randomization was turned off and the background cleaning for the VFAINT observations was turned on. Using the dmcopy tool, the new Level-1 event files were filtered for cosmic-ray events, bad pixels/columns, and other instrumental effects, based on status bits and on-board event grading. To accomplish this, all events with status bits set to nonzero or with ASCA event grades 1, 5, or 7 were excluded. The status bits and event grades are further defined on page 105 of the Chandra Proposers' Observatory Guide (POG) (2009). Finally to construct what is considered a Level-2 event file, we used the dmcopy tool to filter the events for the Good Time Intervals (GTIs). The resulting new Level-2 event file has had all the screening that the SDP would have performed, except that we applied the more recent calibrations, turned-off pixel randomizations and performed background cleaning on the VFAINT observations.

From the new Level-2 event files, we then filtered three copies by specific energy ranges, defined in Table 1. We extracted images of each chip from the 3 major energy band event files in order to effectively perform the computationally intensive processes at their full resolutions (1024 x 1024 pixels). The first of these computationally intensive processes was to create spatial

mappings to account for the exposure variations across each chip. These variations are due to *intrinsic* instrument variations and *extrinsic* telescope aspect variations. Together these variations combine to form the relative exposure map for each chip. (This is an analogous concept to the flat-fielding corrections commonly applied in optical observations.) To construct the instrument map, which accounts for the effective area as a function of position on the detector, the mkinstmap tool was utilized. Although the effective area is energy dependent, we assumed a monoenergetic distribution at 1.5 keV. (A second option would be to use a spectral weighting method. However, this requires using a certain source spectrum *a priori*, which for our unknown background sources would not be of benefit at this step in the processing.) By default, Chandra observes using a Lissajous dither pattern that spans 16 arcseconds from peak to peak. As the Chandra POG (2009) has detailed, dithering serves two important purposes: 1) provides partial exposure coverage in the gaps between chips; 2) smoothes out pixel-to-pixel variations (p. 99). To account for the specific dithering performed during each observation, an aspect histogram was constructed with the asphist tool. Each of these mappings was combined into the exposure map by the expmap tool. Finally, the Level-2 event files for each major energy band in each observation were normalized by the appropriate exposure maps through the dmimgthresh tool.

ii. Source Detection and Extraction

For the detection of the X-ray sources the CIAO detection algorithm, wavdetect was used (Freeman, Kashyap, Rosner, & Lamb, 2002). Wavdetect has been a widely used X-ray source selection tool, having good reliability with crowded fields and identifying extended sources. Kim et al. (2004) mentioned wavdetect's superior performance over alternate CIAO algorithms (e.g., celldetect), and they implemented it as the main detection tool for the ChaMP survey. For wavdetect to operate, the input must be a two-dimensional image, rather than the event files.

Therefore the input images used were the individual 1024 x 1024 pixel images of each chip created from the new Level-2 event files. Within wavdetect, the source significance threshold (sigthresh) was set to 10^{-6}, which represents the threshold below which a source will be rejected. Statistically this value implies that the spurious source rate within an image will be one per million pixels. Additionally the wavdetect command was given a range of wavelet scales to compute scaled transforms. The range included nine scales representing the square-root of two series (1.0, 1.414, 2.0, 2.828, 4.0, 5.657, 8.0, 11.314, and 16.0). These values are in units of pixels and constitute the radii of the Mexican Hat function used in the wavdetect algorithm, approximating the size of the sources that can be detected, where for the ACIS chips 1 pixel = 0.492 arcseconds. An example of the source detection output can be seen in Figure 6, where sources are marked by red ellipses and the image is a noise-free reconstruction of the source cells. From the 90 observations, 449 active chips, wavdetect identified 14,684 sources. However, many of these sources are found at very large angles from the on-axis pointing, and are thus unreliable in their positions or even mis-detections. To increase the reliability of our source list, we will employ field-of-view cuts, discussed below.

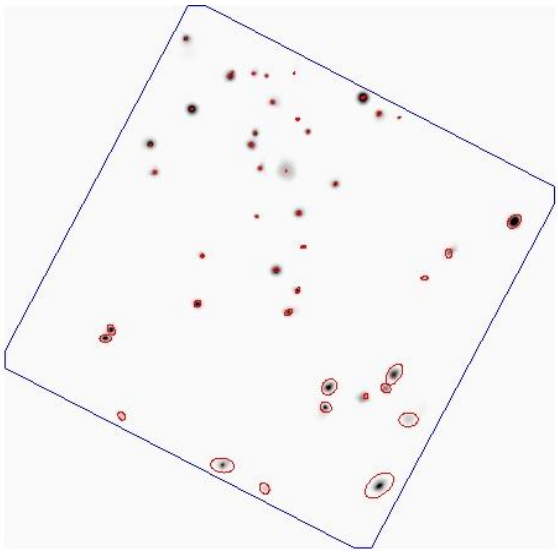

Figure 6: Example of the WAVDETECT Output
Shown here is the noise-free reconstruction of the source cells processed through wavdetect, from ccd3 (I3). Overlaid on the image are the detected sources designated by the red ellipses, where the outer square blue boundary defines the chip. To help in viewing, the ellipse sizes shown here are 3 times larger than the default 39.3% encircled energy radius computed by wavdetect.

For the extraction and determination of the source properties, the dmextract tool was utilized as a more accurate method to obtain source and background counts, rather than those provided in the wavdetect output. As mentioned in the CIAO processing threads,[3] wavdetect is a quite reliable detection algorithm, but should not be the primary, source-count measurement tool. However, wavdetect provides several key parameters needed as inputs into dmextract. One such parameter is the PSF-size estimate for the detected source. Wavdetect's default value for the source's PSF relates to the radius at which 39.3% of the source energy is encircled. This value comes from the 1σ integrated volume of a two-dimensional Gaussian. For the extraction of each source, the encircled energy radius was chosen to be 95% (PSF_{95}), thus the wavdetect PSF-size parameter was scaled up by the ratio of desired percentage (0.95) to 1σ (0.393). The source

[3] http://cxc/harvard/edu/ciao/threads/wavdetect/

counts for each energy band were extracted from the Level-2 event files. The background counts were extracted in annuli sized so that the inner radii were [1.1 x PSF_{95}] and the outer radii were [5 x $(2.21)^{1/2}$ x PSF_{95}]. These radii were chosen to help ensure that an equivalent number of counts would be present in both the source and background regions, providing adequate statistics for the background correction. For the actual extraction of the background counts, the dmfilth task was incorporated into the process to produce source-free background images from which the counts would be extracted by dmextract. Using the dmfilth task, each source was replaced with a Poisson distribution based on the mean of the counts in the background annuli.

iii. Detection Probability Rate

For Chandra, the probability that a real source is missed, or conversely the probability of source detection is a complicated mixture of a source's off-axis angle, source strength, and intensity of the background. At increasing off-axis angles the PSF size increases allowing for a greater number of background sources to be spread within the source region. The relative signal-to-noise (source intensity versus background intensity) thus factors into the ability to discriminate true sources from Poisson fluctuations. These factors influence how the detection probability rate will decrease across the field.

To address the lower-bound of the detection probability, we used the MARX simulator to generate simulated fields of faint sources (~10-20 counts) located at known positions and distances from the aim point. Four separate fields were generated with greater than 100 sources per field. The simulation background was constructed from the longest ACIS-I observation in the sample. All contaminating sources were iteratively cleaned from the field by replacing their counts with a Poisson distribution derived from the global background of the observation. Each iteration was then processed through wavdetect until no source regions were detected above the

10^{-6} threshold. This procedure resulted in a source-free background field having a count density of ~0.1 cnts/pix, which is greater than 90% of the sample observations. The faint sources embedded in this upper-end background rate provided lower-limit quantification for the rates of detection at each off-axis angle. Figure 7 illustrates the arrangement of sources within the ACIS-I array, where the large circle denotes the 10 arcminute radius. Figure 8 shows the significant decline in detection rate as the off-axis angle approaches 10 arcminutes. These simulations focused on the faint source limit and the rate of decrease is a count-dependent function, where the detection probability is less severely affected for brighter sources. Kim et al. (2004) showed similar simulations using Chandra, where they found at the 10 arcminute angle and assuming background intensities of ~0.1 cnt/pixel, that as a source's counts increase from ~20 to ~40 the probability of detection increases from ~10% to 50%, and near the 100 count threshold the probability is back above 90%. Figure 6 shows off-axis locations. In Figure 7, we have plotted some of the simulation data from their paper, showing how changes in the background intensity alone affect the detection probability. All sources in Figure 8 have around 20 counts.

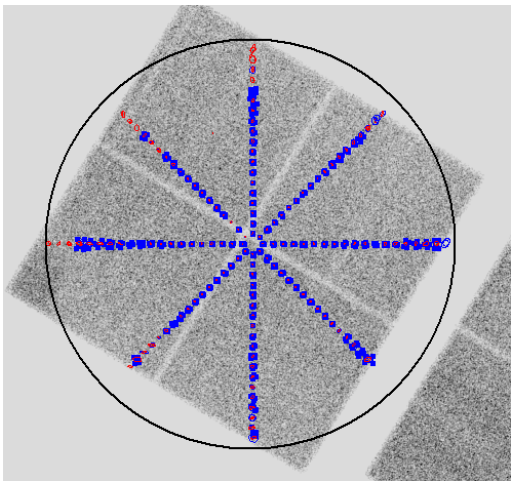

Figure 7: MARX Source Detection Simulation
Shows one simulation field containing the MARX simulated sources (red ellipses) within the constructed background. The detected sources are marked by the blue ellipses, and the black circle denotes the 10 arcsecond radius from the aim point.

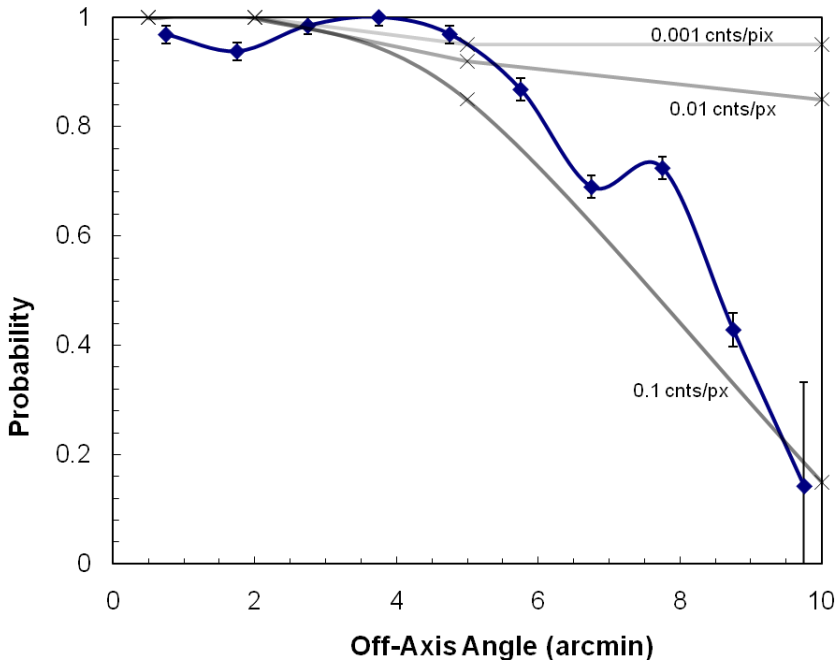

Figure 8: Detection Rate versus Off-Axis Angle
The graph shows the rate of source detection as the off-axis angle increases. All data are based on sources with near 20 counts. The blue line with associated error bars shows the rates compiled from the four simulated fields in this study. The gray lines with cross data points are from the ChaMP survey by Kim et al. (2004) and show the detection rates at four OAAs and at background intensities of 0.1 cnts/pixel, 0.01 cnts/pixel, and 0.001 cnts/pixel (from bottom to top).

iv. Positional Error and Usable FOV

As was mentioned previously, the High Resolution Mirror Assembly (HRMA) of Chandra has given orders-of-magnitude better resolution than many of its predecessors. With sub-arcsecond resolution, Chandra has had the ability to make identifications of the discrete sources contributing to the XRB. However, the superb resolution for on-axis sources quickly degrades at large off-axis angles. The PSF, which for on-axis points is only several pixels wide, can quickly become distended and even take on significant asymmetries at the edge of the FOV; see Figure 4.14 and 4.15 on pages 51-52 in the Chandra POG (2009). To test and determine appropriate restrictions for off-axis angles and usable FOV, we used a representative subset of 10 observations, noted by asterisks in column 1 of Table 3. Figure 9 demonstrates the trend of increasing PSF as a function of off-axis angle for this subset as expected for the full sample. The PSF plotted in this figure is based on that found by the wavdetect detection algorithm, where the PSF plotted is the scaled 95% encircled energy (PSF_{95}) parameter. This data matches well with the calibration tests performed on simulated sources as described in the chapter on the HRMA in the Chandra POG (p. 41-53, especially Figure 4.13). Additionally, wavdetect calculates the 1σ positional uncertainty in both detector and celestial coordinates. The positional uncertainty versus off-axis angle is shown in Figure 10, where the positional uncertainty represents the 3σ total error in arcseconds. Figure 10 further shows that the positional uncertainty also depends on the strength of the source. These results match well with the simulations performed by the ChaMP survey described in Kim et al. (2004, Section 5), where they broke down the count dependence of the positional uncertainty as well as the increasing error with off-axis angle.

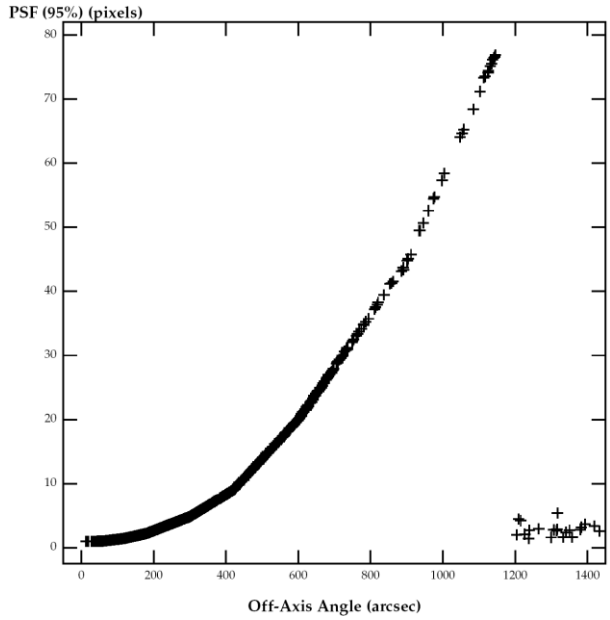

Figure 9: PSF Growth Versus Off-Axis Angle
The relationship between the ACIS PSF versus off-axis angle is shown for the set of sources detected with `wavdetect` from the representative subset of observations. Here the PSF used is the size at 95% of the encircled energy.

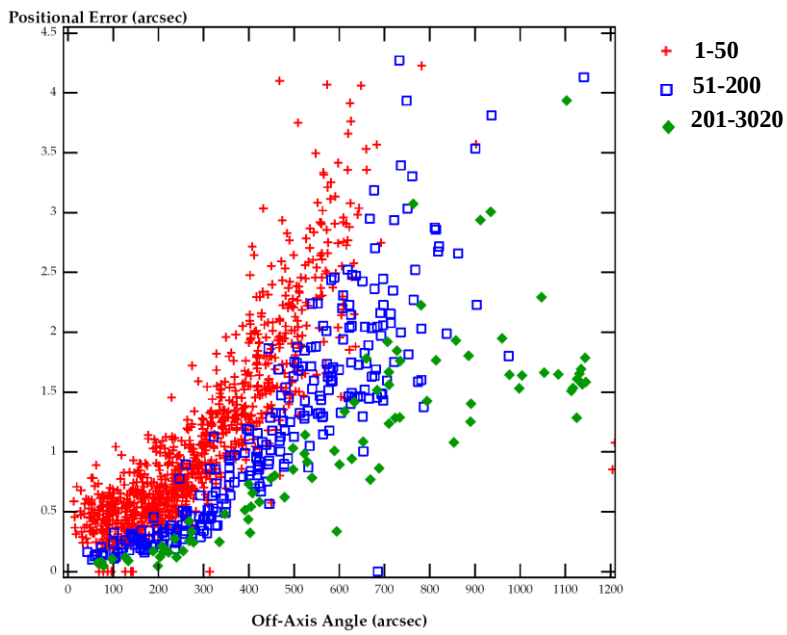

Figure 10: Positional Uncertainty Versus Off-Axis Angle
The sources are broken down by net-counts in 3 interval ranges: 1-50 (red crosses), 50-200 (blue, open squares), and 200-3005 (green, filled diamonds). The dependence on source counts is obvious, the larger the counts the better the positional accuracy. The positional error shown here is the 3σ error computed by the detection algorithm.

These uncertainties, along with the detection probabilities shown in Figure 8, helped to define appropriate FOV criteria by which the present study's sample could be restricted to better constrain the detection completeness levels. Based on these figures, a reasonable cutoff could be made at an off-axis angle of 600 arcseconds (or 10 arcminutes). This value also is appropriate given that the square ACIS-I array has sides of 16 arcminutes, where the aim point on the I3 chip is near the center of the array, resulting in a distance of ~11.5 arcminutes to the corners.

v. X-ray Source Catalog

In addition to the usable FOV refinements discussed above, the sources from the overlapping X-ray observations were cross-matched to identify multiple detections and remove repeated sources. When two sources were detected in separate observations the source with the lowest S/N based on the Broad-band counts was removed. Thus, the off-axis angle cut reduced the catalog to 10,771 sources, while the removal of duplicated sources reduced the final X-ray selected source catalog to 10,207 sources.

C. Multiwavelength Source Correlations

i. Mid-Infrared Spitzer Correlations

As discussed earlier, 65 of our 79 unique (in total 75 of 90) Chandra fields have overlapping Spitzer IRAC observations. The IRAC[4] instrument is an imaging device with four mid-infrared bands: 3.6μm, 4.5μm, 5.8μm, and 8.0μm (designated as channels 1-4, respectively). As the IRAC images a particular field, the targeted aim point is transitioned between two adjacent fields-of-view in the focal plane. Each FOV is imaged simultaneously in pairs, the 3.6μm and 5.8μm is one pair and the 4.5μm and 8.0μm is the second. Due to this physical arrangement and transitioning of the aim point, the FOV for each simultaneous pair is ~5 x 10

[4] http://www.cfa.harvard.edu/irac/

arcminutes. Thus, there is a region of about 5 x 15 arcminutes in size that has coverage in at least two channels, with a 5 x 5 arcminutes overlap for all 4-channels. Figure 11 shows an example of the overlapping detector FOVs for a Chandra and IRAC observation.

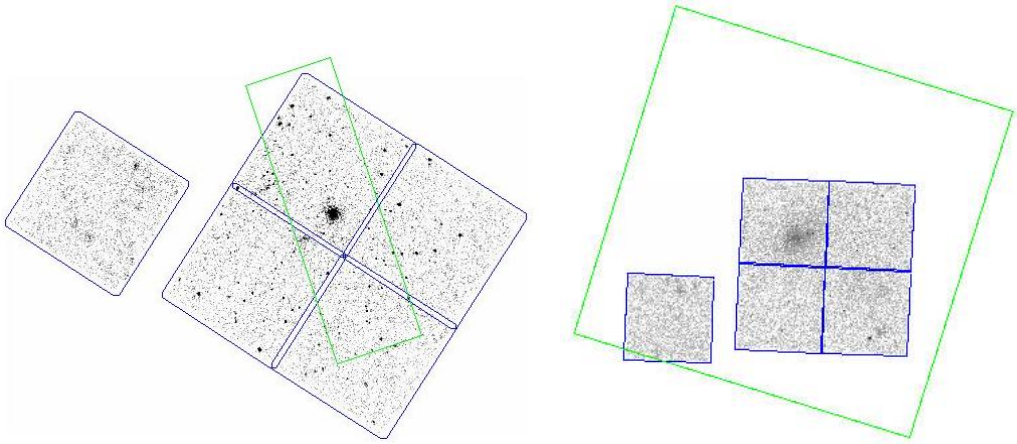

Figure 11: Example of Chandra and Spitzer FOVs
Overlaid as blue squares on images of the X-ray observations, ObsID = 4163 and ObsID=2207, are the active chip regions for ccd0-ccd3 (I-array) and ccd6 (S2). Shown by the green rectangle offset across the X-ray chip regions, is the area of sky seen by the two Spitzer IRAC FOVs, where the area within the rectangle has coverage in at least two channels. The FOV coverage is variable to each observation. Here are examples of the extreme minimum coverage to having full coverage.

For the source correlation and extraction, the IRAF (Image Reduction and Analysis Facility) analysis software was used. Specifically, the `phot` task within the aperture photometry (digiphot.apphot) package was utilized for its ability to not only extract source and background counts, but to centroid on the nearest source within each extraction region. To constrain the centroiding algorithm, two parameter utilities, centerpars and datapars were manipulated to restrict the amount of shift by which the centroid could change the aperture coordinates. Using the fact that the pixel size for the IRAC array is 1.2”/pixel, the centerpars.shift was set to 2.08, to set the maximum search radius to 2.5”. Any X-ray sources for which the nearest centroid on the IRAC detector was greater than 2.5” was flagged, and subsequently was not included in resulting

analyses. [Many of the centroids greater than 2.5" had fluxes equal to the saturation limits listed according to exposure length on page 102 in the Spitzer Observer's Manual (2006).] Also, a signal-to-noise flag was put into place for sources with ratios less than two.

Of the 8695 unique X-ray identified sources with overlapping IRAC observations, 4845 were detected in at least one IRAC band, while 1487 had detections in all 4 IRAC bands. For photometric analyses, we required that the maximum magnitude error in any band be less than 1.25, which resulted in 1025 sources with an average separation of 0.533 arcseconds. Table 4 summarizes the photometric statistics for the IRAC sources, including the breakdown for detections in each band.

ii. Optical SDSS Correlations

The optical correlations came from the seventh public data release (DR7) of the SDSS, where 51 of 79 unique Chandra fields (in total 56 of 90) had corresponding photometric and spectroscopic coverage. The optical source lists were queried directly from the archive instead of reprocessing the raw data; this was opted for due to the high level of uniformly processed data already available through the SDSS archive. To identify the optical counterparts of our X-ray detected sources, we used the SDSS CrossID interface[5] to select the nearest primary object based on our X-ray positions. The positional matching limit was set to a fixed upper-bound value of 5 arcseconds. This value was chosen as a reasonable upper-limit, given the astrometric quality of Chandra and the SDSS. For many of the X-ray sources, especially those near on-axis, this radial search was greater than required, but constituted an adequate region for the X-ray sources farther off-axis. Of the 6201 sources within the SDSS footprint, there were found to be 2327 with an

[5] http://cas.sdss.org/astrodr7/en/tools/crossid/crossid.asp

optical counterpart, where the average separation between X-ray position and optical position was 1.55 arcseconds.

iii. Spectroscopic Correlations

For such a large solid-angle survey, the SDSS provides rather deep spectroscopic completeness: $i' < 19.1$ mag. for the QSO sample[6]. However, for our sample the mean magnitude is $i' = 20.32$, where only 463 of the 2327 matched sources have $i' < 19.1$, and of these 27% (125) have spectra. Additional spectroscopic redshifts were obtained by performing similar radial searches in NED. Of our sources without SDSS spectroscopic redshifts, 94 were obtained from the papers and catalogs available in NED. (Of these 94 NED redshifts, 42 had coverage with SDSS photometry.) Combining the SDSS and the NED samples, our spectroscopic redshift coverage totals 219 sources. Figure 12 shows the redshift distributions for the SDSS and NED sources. We classified the SDSS spectra into three general types: Broad line AGN showing >2000 km s^{-1} broad lines, Narrow line AGN, and "Normal" galaxy spectra showing absorption lines and stellar dominated spectra. The breakdown of the 125 SDSS spectra were as follows: 42 (34%) BLAGN, 30 (24%) NLAGN, and 51 (41%) Normal.

The SDSS archive also contains photometric redshift estimates based on template fitting of source photometry. The SDSS has three estimate techniques to compute the redshift. We incorporated redshifts from all three, based on which algorithm gave the lowest estimated error. Still not all sources in the archive had available photometric redshifts. For our sample, 1396 did, however, the range was restricted to $z_{phot}<0.5$. Figure 13 shows the z_{spec}-z_{phot} correspondence. We combined the photo-z estimates with the spectroscopic sample described below for our subsequent luminosity analyses.

[6] http://www.sdss.org/dr7/index.html

D. Mid-Infrared Versus Optical Correlations

Comparing the photometric SDSS subsample (2327) and the 4-band IRAC subsample (1025), 301 sources had coverage in all 9 optical/mid-IR bands, where 614 had at least 7-bands (all 5 optical and at least 2 mid-IR). Comparing the 4-band IRAC sample with the spectroscopic sample (219), 58 sources had spectroscopic redshifts (32 from the SDSS and 26 from NED), while 92 had spectroscopic redshifts and at least 2-mid-IR bands (46 from SDSS and 46 from NED). Figure 12 shows the redshift distribution for the 4-band IRAC sample.

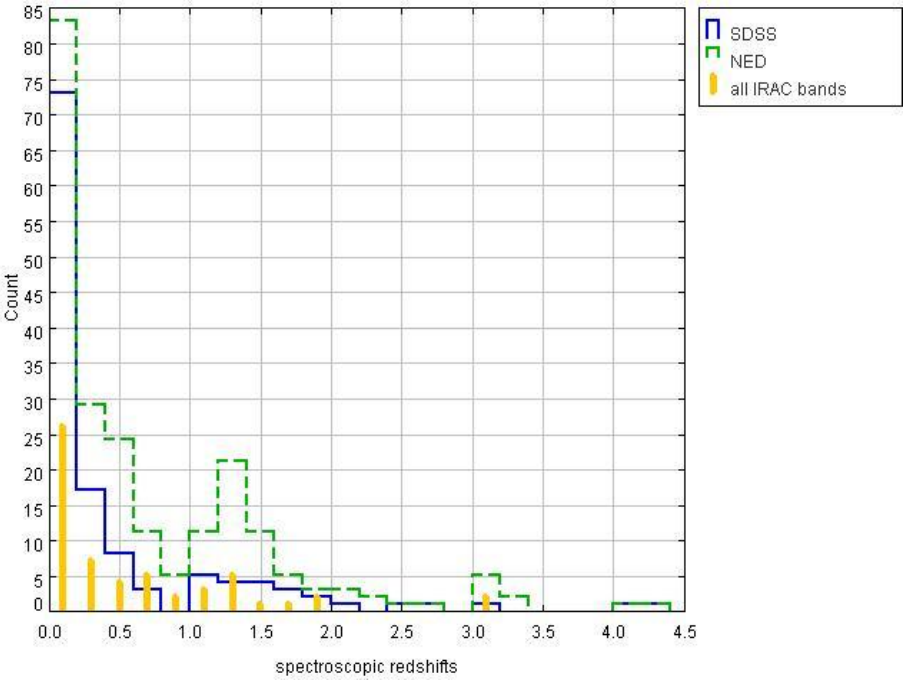

Figure 12: Redshift distributions.
Redshifts include spectroscopic values from the SDSS spectra (solid blue line) and NED database (green dashed line). The redshift sources with corresponding IRAC coverage in all 4 bands are shown as the narrow, orange columns.

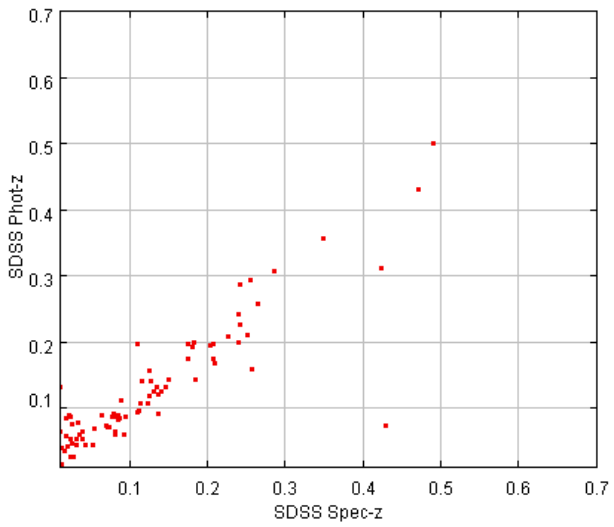

Figure 13: Spectroscopic Versus Photometric Redshifts
Both the spectroscopic and photometric redshifts were obtained through the SDSS DR7.

3. X-RAY PROPERTIES

A. Photometric Properties

i. Hardness Ratio

As was mentioned in Section 2.B.ii, source extraction and the following photometric analyses were performed using the X-ray sources detected from the Broad-band. In order to compare general source properties in a relatively quick sense, we have made use of the classic Hardness Ratio (HR) parameter, which is a relative comparison of the counts observed in two broad bands labeled Hard (H) and Soft (S), where the form is given as

$$\boldsymbol{HR} = \frac{(\boldsymbol{H}-\boldsymbol{S})}{(\boldsymbol{H}+\boldsymbol{S})}. \qquad 1$$

It can be seen from the above formula that an HR > 0 represents a source with relatively more counts in the Hard-band than in the Soft. The more positive the HR-value, the harder the source, which means that the observed flux is dominated by higher energy X-rays. This is the case for the type-2 AGN, where the soft X-rays are obscured and the dominant observed flux is hardened. It can also be seen from the above equation that values with an HR > |1| are nonphysical values. (As a point of observation, I find this type of procedure similar to the color indices (B-V) or (V-R) found often in optical analyses.) In this project, we calculated two HR-values based on different definitions for the H and S-bands, the first with the bands used for source detection, H(2.1-9.5keV) and S(0.3-2.1keV); and the second using the standard ranges of H(2.0-8.0keV) and S(0.5-2.0keV) earlier defined in Table 1. For the majority of sources, the counts used in this calculation were the net counts of the source after background subtraction,

where the background counts are scaled appropriately by the ratio of the source and annulus area:

$$BackgroundCounts = AnnulusCounts \times \frac{SourceApertureArea}{AnnulusArea} \quad . \qquad 2$$

This meant though, that sources that had not been detected due to low counts in the Hard- or Soft-band images alone were now being extracted and background corrected for each range. This yielded some sources with either net-counts that were zero, or negative, which resulted in a non-physical HR value, that is, outside the boundary values of ±1. For sources with single-band (H or S) counts less than 5, the raw counts for that band were substituted into the HR equation. If both bands were below 5 counts, then the HR-value was not calculated.

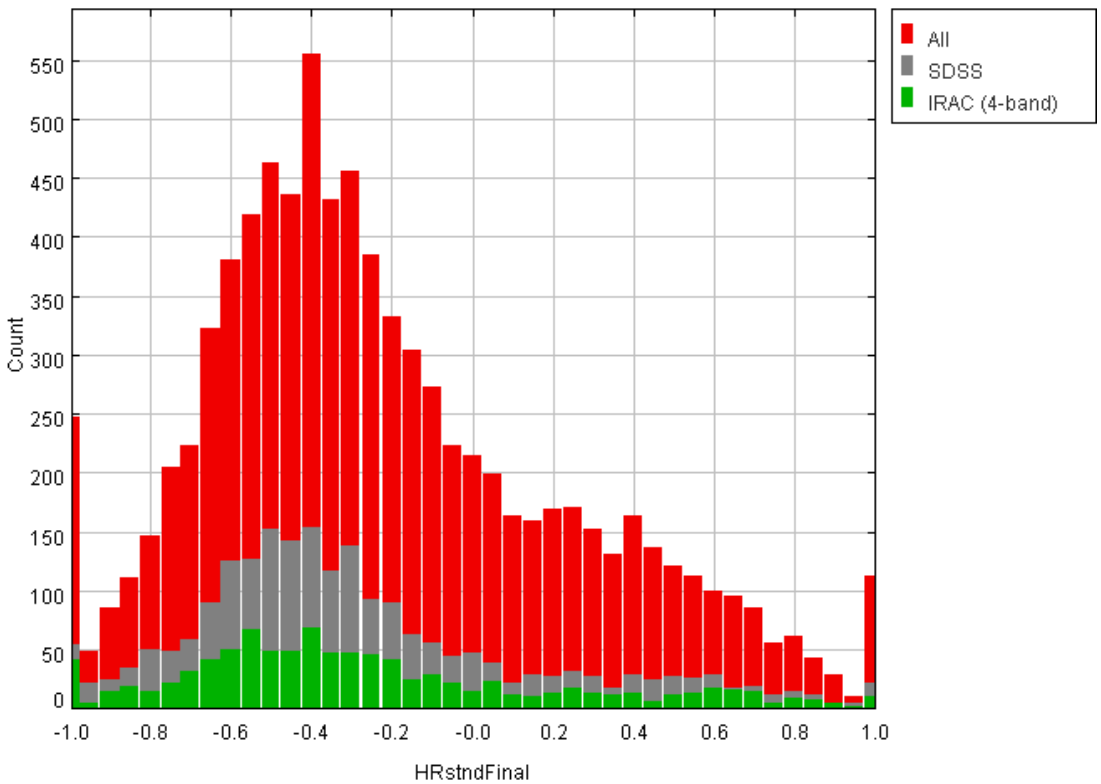

Figure 14: HR Distribution.

Graphed are the corrected HR-values, excluding the duplicate sources between the overlapping fields of observations. The mean value for this sample is at HR = -0.157.

As the final source list, we used the output from the detection algorithm applied on the Broad-band (0.3-9.5keV) images in order to maximize the available source counts. We then extracted the counts, filtering for each of the Broad, Hard, Soft, standard Broad, standard Hard, and standard Soft-bands. Figure 14, shows the source distribution of the standard-band HR-values. A large pronounced peak is seen at approximately HR=-0.4, while the mean for the full sample is HR = -0.157±0.07. However, there is an obvious distribution of hard sources (HR > 0) seen in the full, SDSS-matched, and IRAC-matched samples. From the full and SDSS samples, it appears that the hard-wing may have a peak between 0.2 to 0.4. The full sample breakdown has 2381 sources with an HR > 0, which represents an initial selection pool where candidate type-2 AGN could exist.

ii. Source Flux Determination

In determining the flux of each source we used the modeling capabilities of Sherpa within the CIAO suite. Within Sherpa, we were able to define a general source model to approximate the typical AGN spectral model composed of a power-law and absorbed component. For the power-law component, we chose the XSPEC `powerlaw` model (denoted `xspowerlaw` within Sherpa), which is expressed as

$$A(E) = KE^{-\Gamma}, \qquad 3$$

where the photon-index, $\Gamma = 1.7$, and K is a normalization constant. According to Wang et al. (2004), the Soft-band fluxes are rather insensitive to the photon-index, whereas the Hard-band fluxes (and Broad-band to a lesser degree) are quite sensitive. A photon index of 1.7 was chosen since obscured AGN have $\Gamma \sim 1.4$ (strong reasoning for them having a dominant contribution to the XRB, which also has $\Gamma = 1.4$) and unobscured typically have $\Gamma \sim 1.9$, where we have chosen

a reasonable mid-range value to better account for both AGN types. For the absorbed component of our source model, I used the XSPEC photoelectric absorption model (denoted as `xswabs`). By applying an absorption component, a proper accounting of the Galactic absorption could be achieved, for the direction of each observation field. The Galactic absorption appropriate for each field was obtained using the column density task `nh` under the FTOOLS package, which accesses the neutral hydrogen maps of Dickey and Lockman (1990). The value of each field was derived as a weighted average from a region with radius 0.5 deg.

With the source model defined (`xspowerlaw*xswabs`), the next step was to assign an appropriate instrument model. This allows us to account for the chip variations: first order—the differences in response between front-illuminated (FI) and back-illuminated (BI) chips, and second-order—the internal spatial variations present in each chip. To accomplish these corrections, Sherpa uses a redistribution matrix file (RMF) and an auxiliary response file (ARF). For this analysis, appropriate RMF and ARF files were created for each active chip and for each observation, since temporal variations are also present due to detector degradation effects.

Again, such processing is a tedious procedure, especially when for each source (10,207) the following components must be defined: source model components, appropriate Galactic absorption coefficient, instrument response (applying chip and observation specific RMF and ARF files), effective exposure time (observation specific), and source count rate (to properly scale the model's amplitude). To accomplish this task, I implemented a FORTRAN code that would create Sherpa formatted scripts with all of the appropriate component and parameter definitions for every source, given ASCII files listing the sources and their counts, as well as a template for the global parameters applicable to all the sources on a single chip for a given

observation. After the Sherpa scripts were generated and run, the output was parsed into fits files containing the Broad (0.3-9.5keV), Soft (0.3-2.1keV), Hard (2.1-9.5keV), standard Broad (0.5-8.0keV), standard Soft (0.5-2.0keV), and standard Hard (2.0-8.0keV) fluxes. The average source had a flux of 8.08×10^{-15} ergs cm^{-2} s^{-1} (standard Broad), 3.03×10^{-15} ergs cm^{-2} s^{-1} (standard Soft), and 5.05×10^{-15} ergs cm^{-2} s^{-1} (standard Hard) integrated within their respective energy bands.

B. X-ray Spectral Fitting

Depending on the number of counts for a particular source, we performed various levels of spectral fitting. For all sources the spectral model that we assumed followed the power-law model described above, with an additional absorption component to account for the intrinsic absorption above the known Galactic foreground. For sources with low count rates, that is, less than 50 in the Broad-band, we performed a simple column density estimation described below. For sources with moderate count rates (greater than 50 but less than 200) we performed spectral fitting with essentially one free parameter, the intrinsic absorption, by fixing the power-law photon index, $\Gamma = 1.7$. For all sources with counts greater than 200, we performed spectral fitting with both Γ and intrinsic N_H as free parameters.

The column density (N_H) parameter represents a relative measure of the amount of absorption along the line-of-sight between a source and observer. Given the nomenclature, N_H, the column density is a measurement made relative to the amount of absorption that a column of neutral hydrogen would contribute. Of course, this does not imply that hydrogen is the only factor taken into account; rather the spectral models are based on solar elemental abundances. This measurement is commonly achieved with spectroscopy, given a particular X-ray source's spectrum, through performing a fitting analysis with an assumed power-law of appropriate

photon-index and adding an absorbed component that achieves the maximal fit. However, the analysis followed in this project represents an estimate to the N_H-value, based on the photometric properties of the sources instead of the full spectroscopic fitting process, which can only be done for sources of adequate net-counts. The analysis procedure was similar, though not exactly, to that done by Treister et al. (2004).

The breakdown for our sample was as follows: 364 sources had the necessary counts greater than 200 for the two-free parameter fits, while 1399 sources had counts between 50 and 200 for the one-parameter fit. Selecting only fits that had a quality value of > 0.95, as estimated by Sherpa, there were 313 two-parameter fits and 958 one-parameter fits. Between these two subsets, the percent of obscured sources matched well, with the two-parameter subset having only 6% (18) of the sources with $N_H > 10^{22}$, while the one-parameter subset had 8% (74). For the two-parameter fits, the photon index had an average value of 2.10±0.69 matching the overall softness of the sample. There were 16 sources with a photon index < 1.5. Figure 15 shows the distributions of the photon index for this sample.

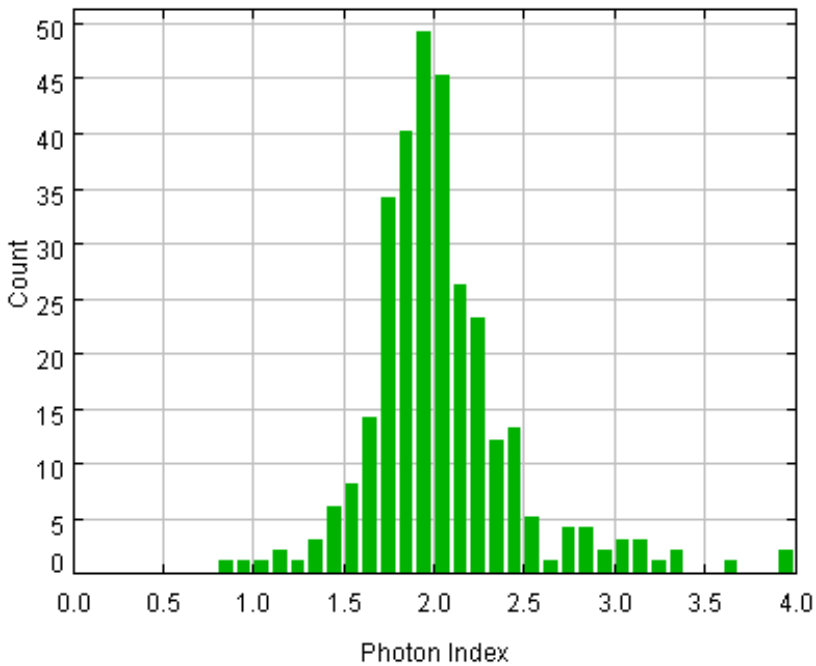

Figure 15: Photon Index Distribution for Spectral Sample
This figure shows the distribution of the photon index for the sample of sources with counts > 200.

Using Sherpa, general source models (absorbed power-laws) were constructed to represent an average type-1 AGN with the historically canonical photon-index of $\Gamma = 1.7$ (Mushotsky, 1984; Turner & Pounds, 1989). The model was then matched with instrument response files (RMF and ARF) to account for the differences between front-illuminated (FI, ACIS-I3) and back-illuminated (BI, ACIS-S3) chips. The absorption parameter was varied over a range representing column densities from $\log N_H = 19$ to 23 by increments of $\log(N'_H/N_H) = 0.5$. Using the `fakeit` command, the model data were generated for each of the parameter sets and counts were extracted for the Hard and Soft bands. Using this data, Figure 16 demonstrates the effect of absorption on the HR-values. For comparison, we also have graphed the same model given a $\Gamma = 1.4$. All parameter sets converge quickly at increasingly positive values.

Next, the spectral model now defined in terms of N_H and HR, were fit with spline functions in order to generate an estimation relationship. The spline functions were then sampled at intervals of 0.005 in the logN_H axis, which resulted in a relationship grid between the amount of absorption and the resultant HR-value for a source on a FI or BI chip for either a canonical AGN or a hard-spectrum AGN. Thus, for every source an $N_H^{1.7}$ estimate was assigned based on the actual measured HR-value. Figure 16 shows the absorption distribution, including a similarly derived curve for a photon index of 1.4 for comparison. As can be seen from Figure 16, the defined models have lower-limits to the HR-value that can be evaluated, which means that sources with measured HR-values below these limits will not provide an estimate. The lower-limits for the $\Gamma_{1.7}$ models are -0.62 (BI) and -0.41 (FI). For the $\Gamma_{1.7}$ estimation, 40% (2183 of 8444) would be classified as type-2 AGN having logN_H > 22.

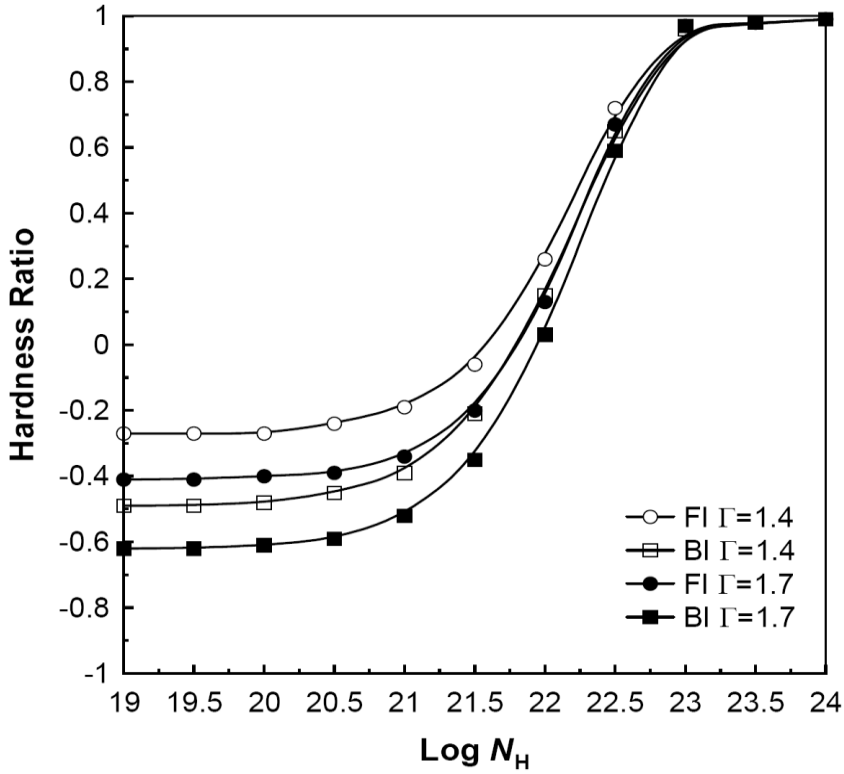

Figure 16: Effects of Absorption on Hardness Ratio
Graphed are the effect on the Hardness ratio when varying the amount of absorption on two power-law models: Γ = 1.4 (circles) and Γ = 1.7 (squares), each with two instrument response factors: Front-Illuminated (FI) and Back-Illuminated (BI) chips. It is noted that as increasing absorption (obscuration) is encountered, the energy spectrum hardens (or tends toward larger HR values). Physically this can be explained by the preferential obscuration of the softer X-rays, which leaves relatively more hard X-rays escaping to reach us. Filled points represent sources on BI chips, while open points are for sources on FI chips. The lines represent B-spline interpolations of the Sherpa model-produced data.

The effect of redshift on a potential AGN source with Γ=1.7, is shown in Figure 17 following the HR- N_H relations. As can be seen, as the obscuration increases the HR value hardens as the softer X-rays are obscured first. At any given column density, an increase in redshift softens the HR value as the hard X-rays are shifted down into the softer energy range, or at any given HR-value the column density must increase as the redshift increases.

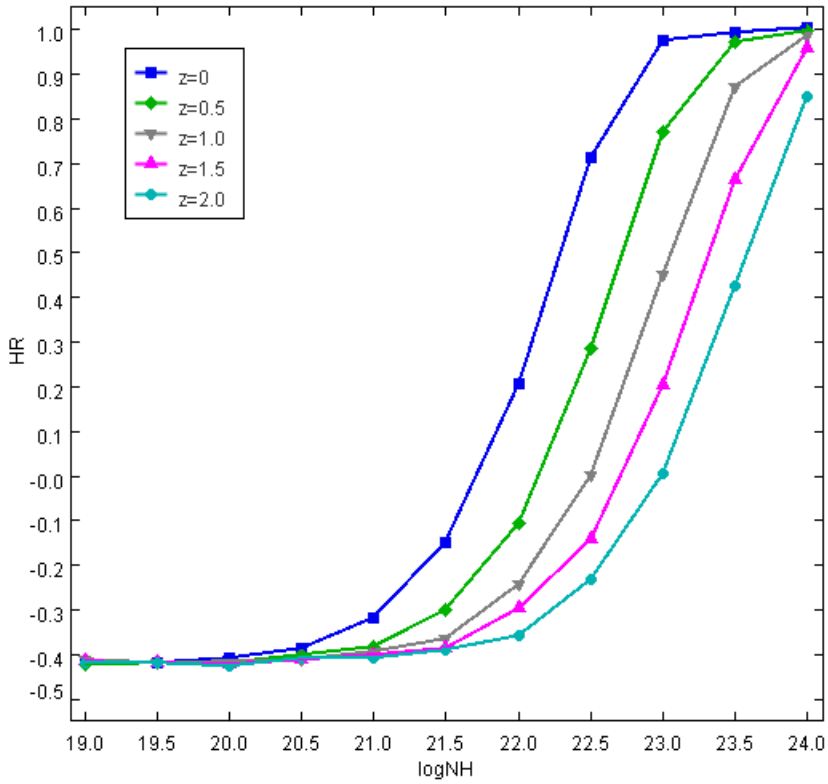

Figure 17: Redshift Effect on the Hardness Ratio and Column Density
The HR-NH relation is shown following a source with Γ=1.7 on a front illuminated chip. The variation with redshift is shown.

4. MULTIWAVELENGTH SOURCE PROPERTIES

In the following section, we analyze and compare various X-ray, mid-infrared, and optical selection techniques testing to what extent they select sources from the same populations. We will use the correspondence between optical and mid-infrared AGN selection techniques test any correspondences among the X-ray source properties.

A. Spitzer IRAC Mid-Infrared Characterization

i. Mid-Infrared AGN Source Properties

Following the source extraction method described in Section 2.B.ii, the X-ray source lists were used to extract the infrared photometry of correlating sources within the overlapping IRAC-channel fields. Of the 10,207 unique X-ray identified sources, 4845 were detected in at least one IRAC band. As noted in Section 2.C.i, there are two FOVs for the IRAC array, one for channels 1-3 and one for channels 2-4. Thus for the channels 1-3 FOV, there are 2,228 common sources in the full sample, and for the channels 2-4 FOV, there are 2,357 common sources. The overlap of these fields contains 1,487 sources with detections in all 4 IRAC bands. Though detected, many of the sources still had poor S/N and large photometric errors, thus a magnitude-error cut (<1.5 mag) was utilized to improve the sample quality, resulting in final sample of 1,025. This higher quality sample will be used in the following analyses. Table 4 summarizes the photometric statistics for the IRAC sources, including the breakdown for detections in each band.

ii. Mid-Infrared AGN Selection: Infrared Power-law Selection

Previous studies by Barmby et al (2006) and Alonso-Herrero et al. (2006) used infrared power-law (PL) criteria to select samples of AGN. Following similar procedures, we used power-law fits ($f_\nu \sim \nu^\alpha$) to the IRAC flux densities as a simple discriminator between AGN-dominated and stellar contaminated SEDs. In the mid-infrared, AGN-dominated galaxies will have red power-laws with smaller power-law indices (α), while those that have higher stellar contributions will have larger-index, inverted or blue power-laws, where stellar-dominated sources have indices of α~2. We used a linear least squares fit to IRAC data using the $\log(f_\nu) \sim \alpha_{IR}\log(\nu)$ relation. We then applied a threshold for acceptable fits with a probability <0.05 from the F-test. Figure 18 shows the histogram of the resulting 336 power-law indices. There is an obvious dichotomy between the red and blue power-law populations, which are divided cleanly at α_{IR} ~0. This natural break in our data was the same cut Barmby et al (2006) applied to their sample in order to separate red and blue sources. The red power-law population (where $-3.5 < \alpha_{IR} < 0$) contains 43% (144 of 336) of the sources and is centered on a mean of -1.463±0.05. The blue power-law population contains 54% (180 of 336) and is centered on a mean of 1.377±0.03.

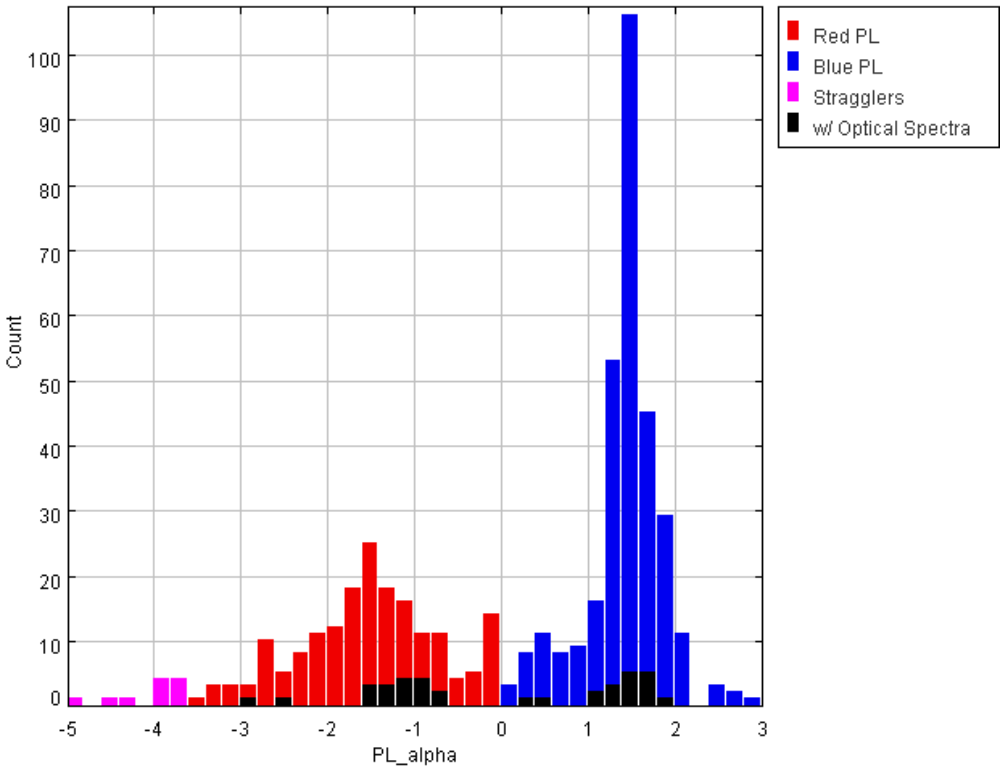

Figure 18: Distribution of Mid-Infrared Power-Law Slopes.
Blue and red slopes are divided around an α=0. A population having extremely red power-laws can be seen at α>–3.5. The black histograms show the few sources with SDSS spectra showing the same dichotomy and following well within each population's range of power-law slopes.

To check our initial conditions, that red PL sources should be AGN dominated and blue PL sources should have noticeable stellar contamination, we compared the distribution of the SDSS spectroscopic sources. Though only 17 SDSS sources fit the requirements: detections in all 4 IRAC bands and fits with probability<0.05, the expected dichotomy still exists in α_{IR} as can be seen from the small black histograms in Figure 18. Seven sources fell inside the red sequence and are all classified as BLAGN, including two Seyferts at z=0.24 and 0.43, and five QSOs at z=1.02 to 1.87. Ten sources fell inside the blue sequence and include galaxies. The spectroscopic populations peak at α_{IR} = -1.02±0.09 (red) and α_{IR} =1.86±0.35 (blue).

Two other interesting features of Figure 18 can be seen. The drop-off at α_{IR} >2 occurs where sources should be stellar-dominated and at the upper end of the blue-sequence of stellar-contaminated sources. The last feature is what appears to be a possible third population, a seemingly red-straggler group composed of 6 sources (1.5% of total), existing in the range -3.5 > α_{IR} > -5.25. The interesting nature of this last group is that several previous studies (Alonso-Herrero et al., 2006; Rigby et al., 2005; Stickel et al., 1996) have seen steep optical-IR slopes out to only -2.8, which are discussed as a probable limit for AGN SEDs. Here we have found a small population that could extend this limit.

Testing the X-ray properties for the power-law galaxies, we found no correlation in the HR-value expected for the populations of either red or blue PL sources; neither is any correlation in the α_{IR}-value for either hard or soft X-ray sources.

iii. Mid-Infrared AGN Selection: Color-Space "Wedge" Technique

Using the "wedge" diagnostic procedures of Stern et al. (2005) and Lacy et al. (2004), we have tested the relative overlap of their selection abilities on X-ray selected samples, and whether there are any distinguishable X-ray characteristics isolated by their mid-infrared criteria.

Figure 19 shows the photometric conditions of Stern et al. (2005) as applied to the mid-IR magnitudes of our sample. The three boundary lines are given by the following inequalities:

$$\text{a)}\ [3.6]-[4.5] > 0.2*[5.8]-[8.0]+0.18$$

$$\text{b)}\ [3.6]-[4.5] > 2.5*[5.8]-[8.0]-3.5$$

$$\text{c)}\ [5.8]-[8.0] > 0.6 \qquad 4$$

Within the full sample (1025 sources), their selection criteria isolated within the "wedge" 273 sources (27%). Of these, 96 had an HR > -0.2, which is 30% (96 of 319 hard X-ray sources

with IRAC coverage) and only slightly more than expected from a random sample. The selected sources also had comparable X-ray fluxes to the full sample ~10^{-14}. Thus, Stern's criteria did not effectively select any particular X-ray parameter.

Testing the Stern selection criteria versus redshift, we find that at high redshifts (z > 1), the selection criteria have a higher efficiency of selecting AGN 71% (10 of 14), where the parent population has 27% selection efficiency (273 of 1025). At z<1, though, there is no greater selection than would be expected from a random sample 25% (80 of 324).

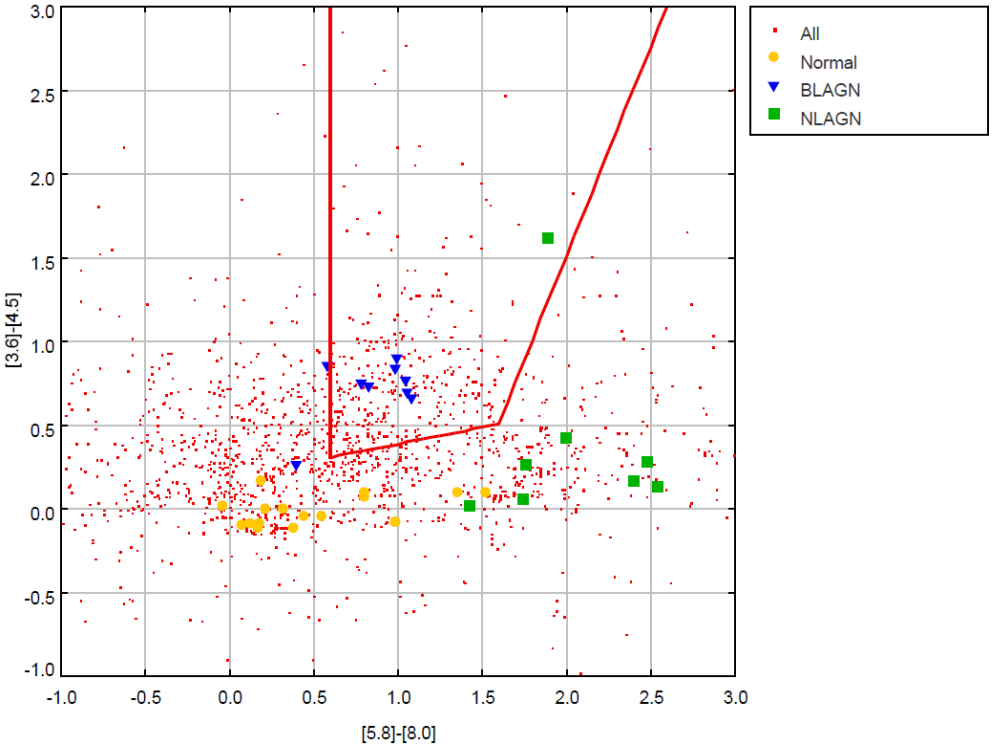

Figure 19: Mid-Infrared AGN Selection Criteria by Stern et al.
This figure shows the color-color AGN "wedge" selection of Stern et al. (2005). All of our sources with 4-band IRAC photometry are plotted as the small, red dots. The "wedge" efficiently discriminates between the BLAGN and NLAGN/Normal populations.

Figure 20 shows the photometric conditions of Lacy et al. (2004) as applied to the mid-IR fluxes of our sample. The three boundary lines are given by the following inequalities:

$$\text{a)}\quad \log\left(S_{5.8}/S_{3.6}\right) > -0.2$$

$$\text{b)}\quad \log\left(S_{8.0}/S_{4.5}\right) > -0.2$$

$$\text{c)}\quad \log\left(S_{8.0}/S_{4.5}\right) < 0.8 * \log\left(S_{5.8}/S_{3.6}\right) + 0.5 \quad . \qquad 5$$

Within the full sample, the selection criteria isolated 566 (55%) sources. Within the spectroscopic defined classes, all BLAGN and only 1 "Normal" galaxy were included in the wedge, while all NLAGN were excluded from the wedge. Having already noticed the close correspondence between IR power-law and spectral type, it is not surprising that all but one red power-law source is selected by the wedge, 18 of 180 blue power-laws are selected (significantly below random effects), and all of the red-straggler power-laws are selected. We also find that Lacy's criteria show increasing flux dependence with decreasing wavelength, where in the 3.6μm band faint sources (with magnitudes > 17, which is the mean) have a selection rate of 91% (174 of 192). Bright 3.6μm sources on the other hand have a selection rate of 47%. As you proceed toward longer wavelengths, the bright source selection rates remain consistent, but the faint end decreases until in the 8.0μm band the rate is 65%. This trend is expected following the efficient selection of red power-law AGN, where by definition their flux rises toward longer wavelengths.

Of the 566 sources selected from the full sample, 199 had an X-ray HR > -0.2, which is 62% (199 of 319 hard X-ray sources with IRAC coverage) and only slightly more than expected from a random sample. However when testing the "wedge" criteria against hard X-ray flux, we find a significant trend toward selecting brighter sources (opposite the IR flux trend). When the X-ray sample is divided around its mean hard flux, $F_{2.0\text{-}8.0\ \mathrm{keV}}$ ~2×10^{-15} ergs/cm^2/s the brighter

(fainter) subsample has a selection rate of 67% (45%). When the flux is increased (decreased) by a decade, the selection rate goes to 71% (38%).

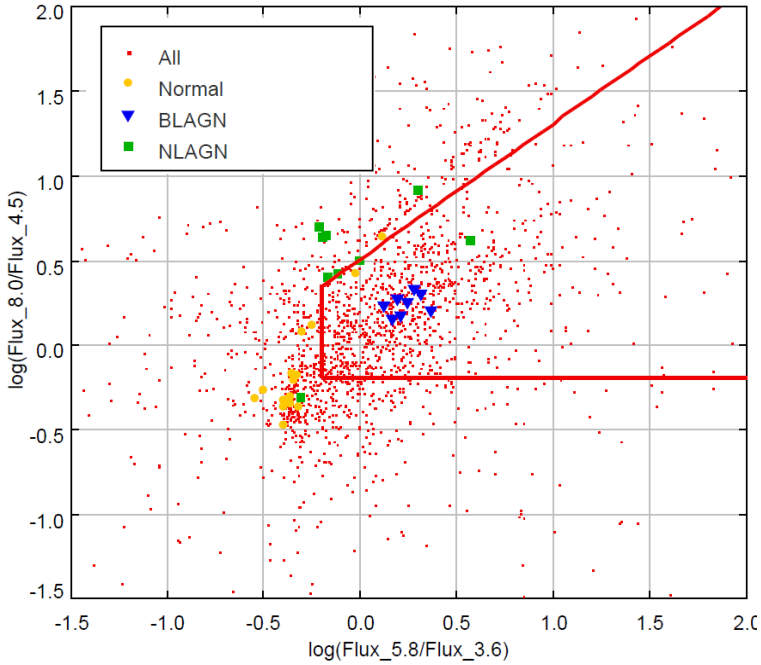

Figure 20: Mid-Infrared AGN "Wedge" Selection by Lacy et al.
This figure shows the color-color AGN "wedge" selection of Lacy et al. (2004). Sources are plotted following the same distinctions as Figure 19.

In comparing these two IR-selection methods, Lacy's criteria selected approximately two times the number of our X-ray selected sources, 57% versus just 27% for Stern's criteria. This larger factor for Lacy's criteria is in spite of it having a smaller per unit color coverage (by ~1.4 times). However, within both IR color-spaces, the X-ray selected sources are distributed rather homogeneously with regards to both the HR-values and the X-ray-to-infrared flux ratio (f_x/f_{ir}). Figure 21 shows the distribution of varying ranges of the X-ray column density parameter oriented within the Stern wedge-criteria. There is no significant clustering or population selected by the color criteria defined by Stern, or by extension the Lacy criteria.

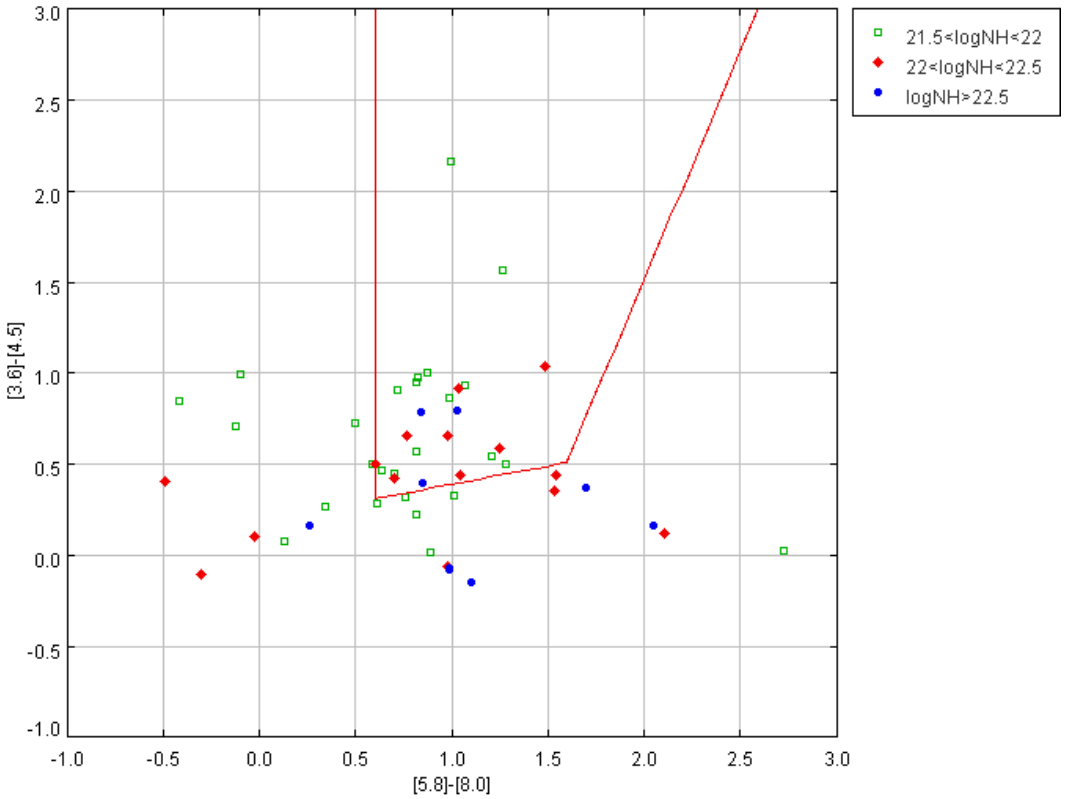

Figure 21. X-ray Column Density Distribution in Stern IR color space
Using the X-ray spectroscopic sample we have graphed the distribution of column density within Stern's mid-IR color wedge. Here we find no preferred clustering.

The fact that both "wedge" techniques heavily favored selection of the BLAGN, as opposed to the X-ray selected NLAGN sample, signifies that solely IRAC based selection criteria may miss significant numbers of low-luminosity or obscured AGN that are host-dominated (Brusa et al., 2010).

B. Optical Source Properties

Within the 56 X-ray observations (51 fields) that overlapped the SDSS coverage, there were 6201 sources, of which 2327 had an optical counterpart within the radial search region. Their *r*'-band magnitudes range from ~9.6-27.6, and their mean color $\langle g'-r' \rangle = 0.78 \pm 0.02$.

i. Optical AGN Selection: Optical Power-law Selection

Following similar procedures, as we did for the infrared power-law selection, we performed power-law fits ($f_\nu \sim \nu^\alpha$) on the SDSS flux densities to discriminate between the sources of emission in our AGN sample. In the optical regime, AGN-dominated sources will have blue power-laws (larger α), which decrease as the host galaxy light contaminates and then dominates the spectrum (which is an opposite sequence as the infrared power-laws, whose consequence will be discussed in a later section). Figure 22 shows the distribution of optical power-law slopes for the spectroscopic sample. There is a clear distinction between the BLAGN and Normal sources. The NLAGN subset falls between the two, but with an obvious distribution of their own. This boundary region where the NLAGN exist would be the best region for identifying obscured AGN candidates. Further evidence for this is shown in the comparison between optical and infrared power-law slopes discussed below.

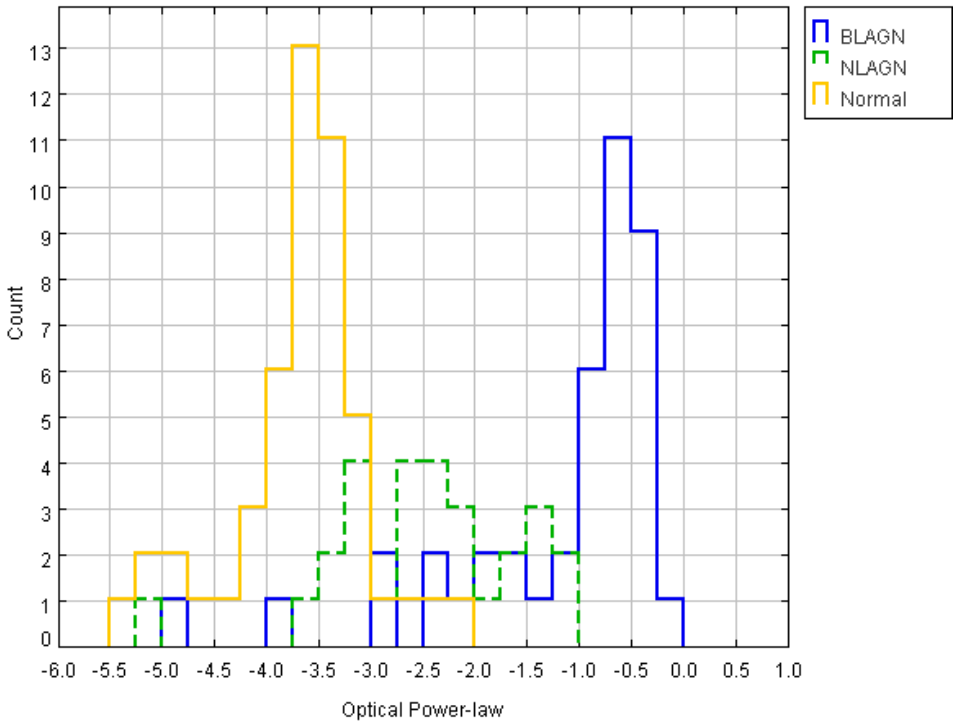

Figure 22: Optical Power Law Distributions
This figure shows the optical power-law distributions for the three spectral classifications: the BLAGN peak at larger values, the Normal galaxies peak at the lowest values, and the NLAGN peak in-between.

ii. Optical AGN Selection: X-ray-to-Optical Flux Ratio

Figure 23 plots the *r*'-magnitude versus the Broad X-ray flux. The lines represent constant X-ray-to-optical flux (f_x/f_r) ratios. The flux-ratio relation followed came from Green et al. (2004), where the ratio was calculated from the Broad X-ray flux and the SDSS *r*'-magnitude by the following equation:

$$\log\left(\frac{f_x}{f_{r'}}\right) = \log(f_x) + 5.67 + 0.4r' \quad . \qquad 6$$

This relation follows also the earlier works Manners et al. (2003) and the foundational work by Maccacaro, Gioia, Wolter, Zamorani, & Stocke, (1988). Because X-ray emission is a hallmark of AGN activity, where AGN-dominated sources are predominantly found in the region

with $f_x/f_r > 0.1$, and stellar dominated (including hot stars) are normally limited to $f_x/f_r < 0.1$. From our sample 1839 of (2424, 76%) had flux ratios > 0.1. Also, for our sample the mean ratio was $\log(f_x/f_r) = -0.178$, which is close to what the ChaMP survey found, $\log(f_x/f_r) = -0.15$ (Green et al., 2004). For sources with $f_x/f_r > 0.1$, the mean HR = -0.287 ± 0.40; where those with $f_x/f_r < 0.1$, had an HR = -0.439 ± 0.45.

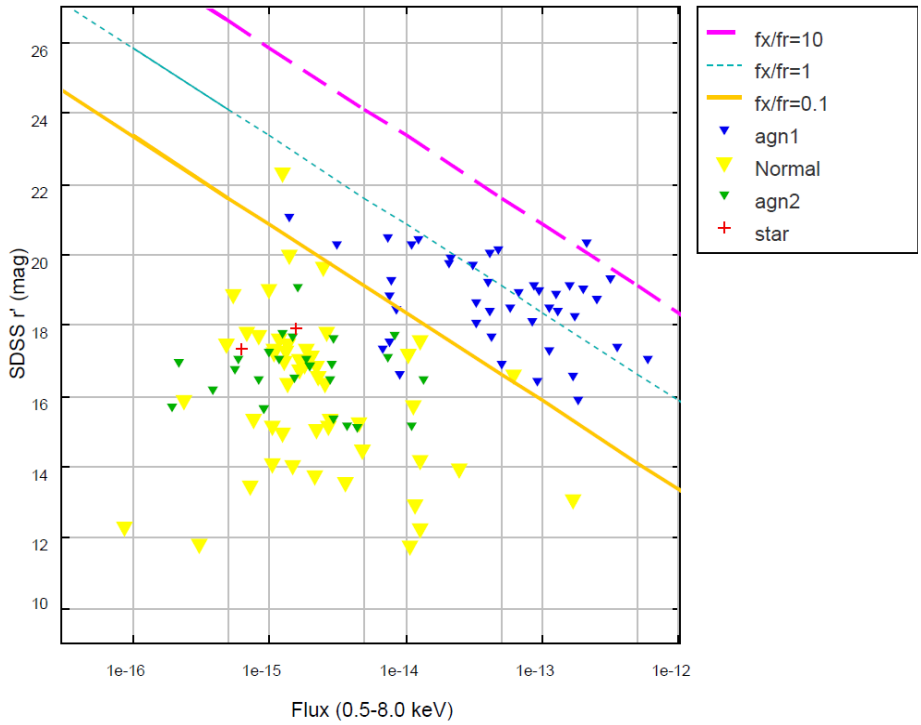

Figure 23: Optical Magnitude versus X-ray Flux
This figure plots the *r'*-band SDSS magnitude versus the broad-band X-ray flux (in units of ergs cm^{-2} s^{-1}). The diagonal lines demarcate constant X-ray-to-optical ratios of 0.1, 1.0, and 10 (from lower left to upper right).

We confirm a strong correlation between Hard X-ray Luminosity (2.0-8.0 keV) and the X-ray-to-Optical flux ratio for optical type-2 AGN, which is similar to that found by (Fiore et al., 2003; Brusa et al., 2010). Figure 24 shows trend-lines for the NLAGN, Normal galaxy, and total spectroscopic samples. The linear relations for the NLAGN and Normal samples overlap within errors, with the NLAGN have a smaller dispersion as evinced by their R-values, 0.647 and 0.736,

respectively. The BLAGN are obviously clustered around the point (10^{44},0.2), and reinforced by an R-value of ~0.3. The X/O ratio of the Normal and NLAGN objects, which are lacking any broad lines in their spectra, can be considered, under unification scenarios, to be an approximation of the nuclear X-ray to galaxy host light ratio.

$$\text{Normal: } XO=0.428L_x - 20.245 \quad R=0.647$$

$$\text{NLAGN: } XO=0.400L_x - 18.995 \quad R=0.736$$

$$\text{ALL: } XO=0.552L_x - 25.145 \quad R=0.880 \qquad 7$$

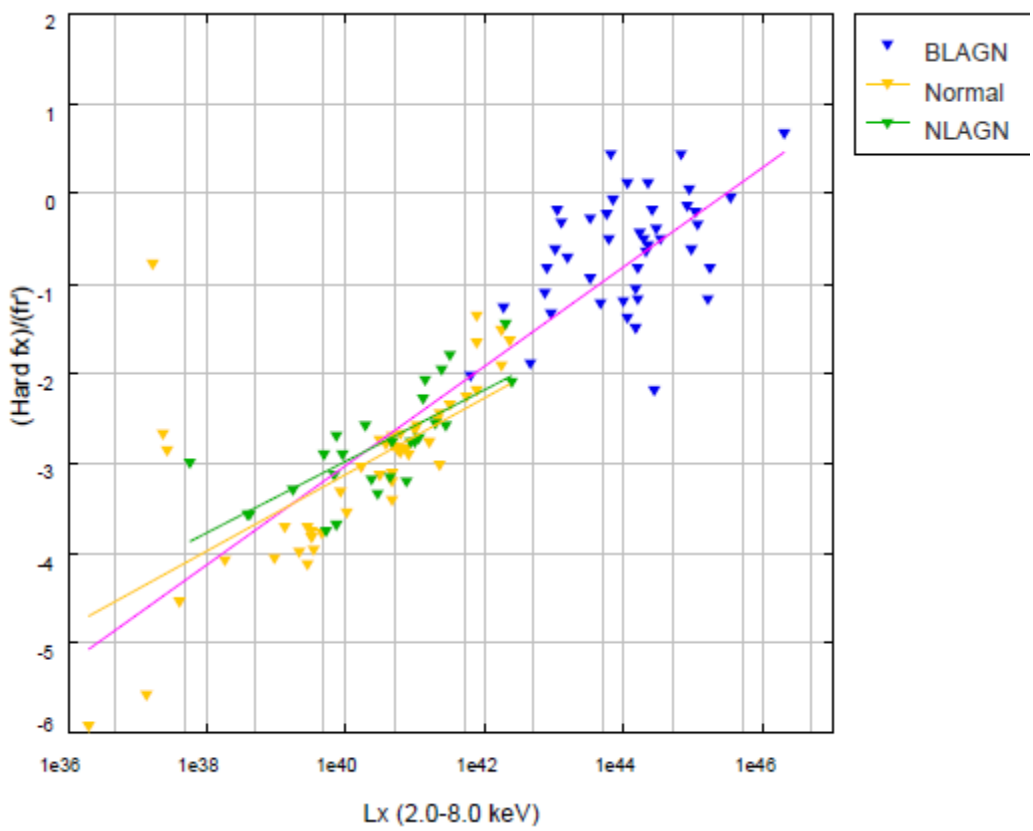

Figure 24: X-ray-to-Optical Flux Ratio versus Hard X-ray Luminosity
This figure plots the ratio of X-ray and optical fluxes versus the X-ray luminosity in the hard-band, for all SDSS sources with spectroscopic redshifts and classifications. The Normal (yellow) and NLAGN (green) subsamples overlap in the lower-left quadrant, while the cluster of BLAGN (blue) sources are in the upper-right.

C. Optical-Infrared AGN Selection: The α_{Opt}–α_{IR} Relation

As previously discussed and illustrated the optical and infrared power-law methods were rather efficient at distinguishing between various sources of emission in our sample. Similarly, color-color techniques also serve to distinguish among the various source types, but are restricted to making use of 4 photometric bands. As Hao et al (2010) noted, by plotting both the power-laws together, an equivalent parameter space to the color-color plot can be formed utilizing more than 4 bands.

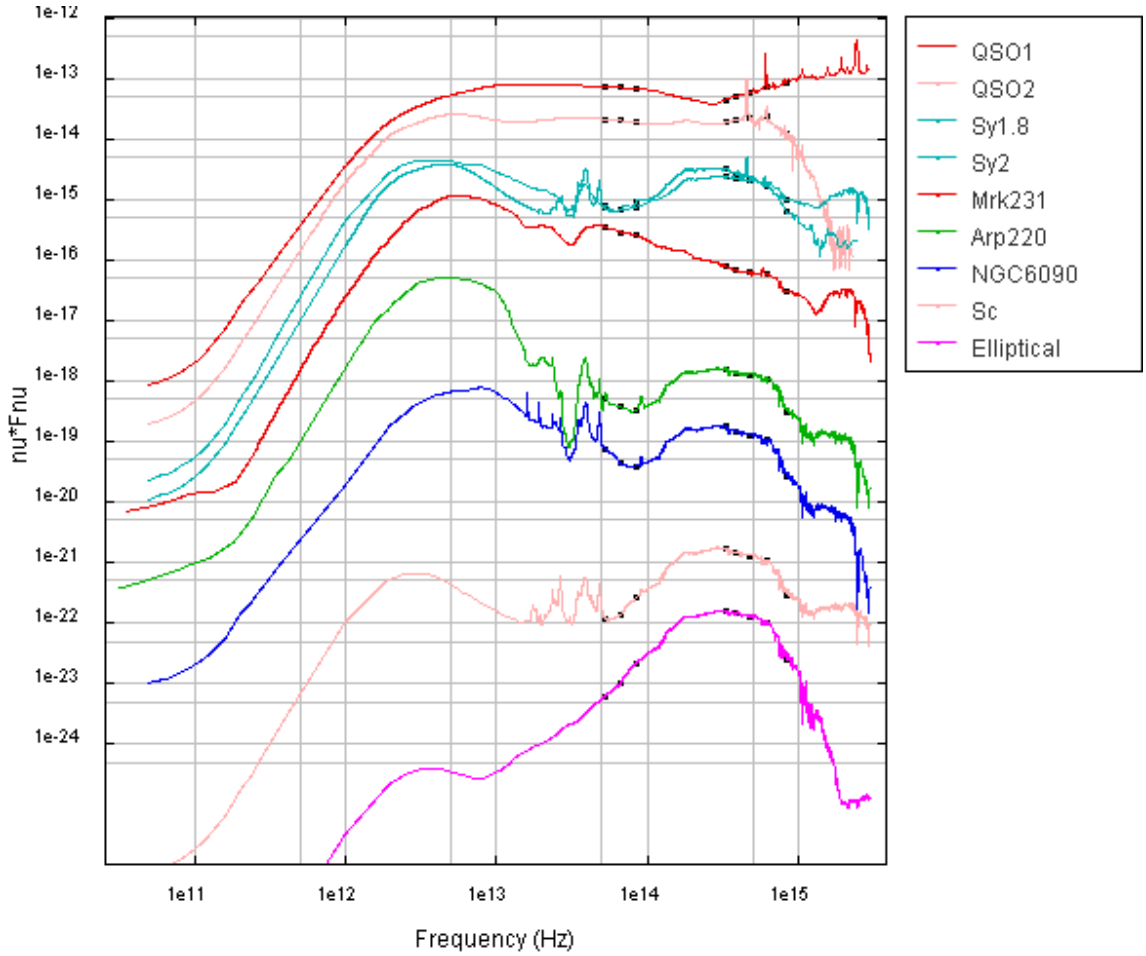

Figure 25: SED Templates of AGN, Starburst, and Normal Galaxy Types
This figure plots 9 template SEDs illustrating the variation in infrared and optical power-law slopes. The templates were taken from the compiled library of Polletta et al. (2007).

The optical bands of the SDSS and mid-infrared IRAC bands are suitably positioned to take advantage of distinguishing between galaxies dominated by the 1.6μm stellar bump and those dominated by the non-thermal AGN emission. Figure 25 shows a variety of AGN, starbursts, and normal galaxy templates. The photometric bands of the four IRAC channels and the five SDSS filters are shown as the points along the SED profiles. Easily visible are the subsample of Normal galaxies having red optical and blue infrared slopes. This large reversal between slopes stems from the relative inversion point around the 1.6μm stellar bump. Figure 26 shows the α_{Opt}–α_{IR} parameter space with the sample of spectroscopic sources having also IRAC coverage has been plotted. The power-laws for numerous template SEDs are also present to highlight the various types. For typical type-1 AGN, dominated by a power-law, the slopes are clustered around smaller values. For the transitional classes and the obscured type-2 classes, the power-law emission of the accretion disk begins to give way to the black-body emission of hot dust. The template SEDs for Seyfert 2 and Seyfert 1.8 objects follow this trend as they are found along the path between the clustered Normal sources (including E0 and Sc templates) and the BLAGN (including QSO1 templates). The third cluster of templates, Arp220, N6240, and N6090, are all starburst-dominated SEDs, while the Mrk231 template, a composite type-2 QSO and starburst SED sits appropriately along the path between them and the QSO2.

The templates labeled Sy2, Sy1.8, Mrk231, and QSO2 represent templates that represent type-2 AGN. These sources, found along the boundaries of the three distributions represent the sources with greater obscuration of the dominant emission region. The parameter space bounded by the box where $-2 < \alpha_{opt} < -1$ and $-1.5 < \alpha_{IR} < 0.5$ would seem to be the best region to search for obscured sources. We note that of the above criteria the α_{opt} criteria range is the more restrictive

of the two and has less overlap with other distributions. If we combine our X-ray obscuration parameters, maybe this would also isolate the best candidates for obscured type-2 AGN.

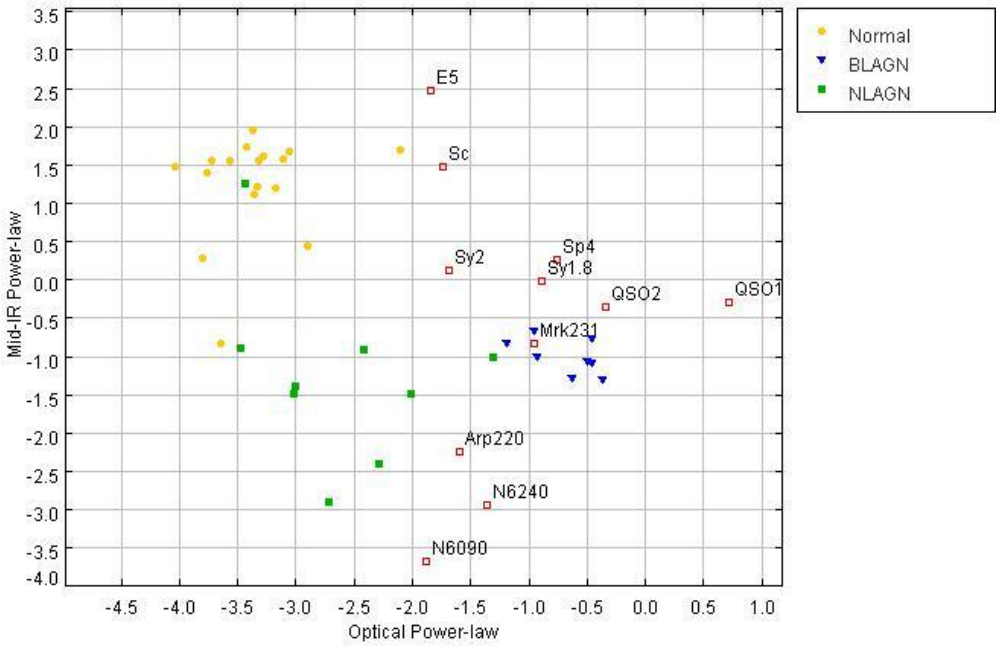

Figure 26: Optical Power-law versus Mid-Infrared Power-law
This figure plots the power-law "color-color" space analog. Here we have shown the spectroscopically classified source populations, plus several SED templates as they would appear in this parameter space.

D. Optical-Infrared AGN Selection: IRAC-SDSS Color Wedge

Since mid-2009, Spitzer ceased "cold" missions, with its liquid helium coolant spent, and entered into "warm" mission status. This means that the IRAC detector's longest wavelength channels, the 5.8µm and 8.0µm, can no longer operate in the midst of the ambient heat. However, the two shorter wavelength channels are available for operation. This means that the mid-infrared color-color "wedge" diagrams, which require all four channels can no longer be utilized by new observations. Here we have used our subset, along with the matched sources from the Stern criteria to demonstrate the use of an IRAC-SDSS color-space as a feasible option. Of course, the optical filters of the SDSS could be substituted for other analogous optical filters.

Testing several relations between the [3.6], [4.5], *u'*, *g'*, *r'*, *i'*, and *z'* filters, we found two relations that seemed to group the Stern selected sources as well as maintain the distinction between the BLAGN and NLAGN/Normal subsets. Figure 27 uses the IRAC channels and the nearest Sloan filter, *z*', while Figure 28 uses the Sloan *i'* filter.

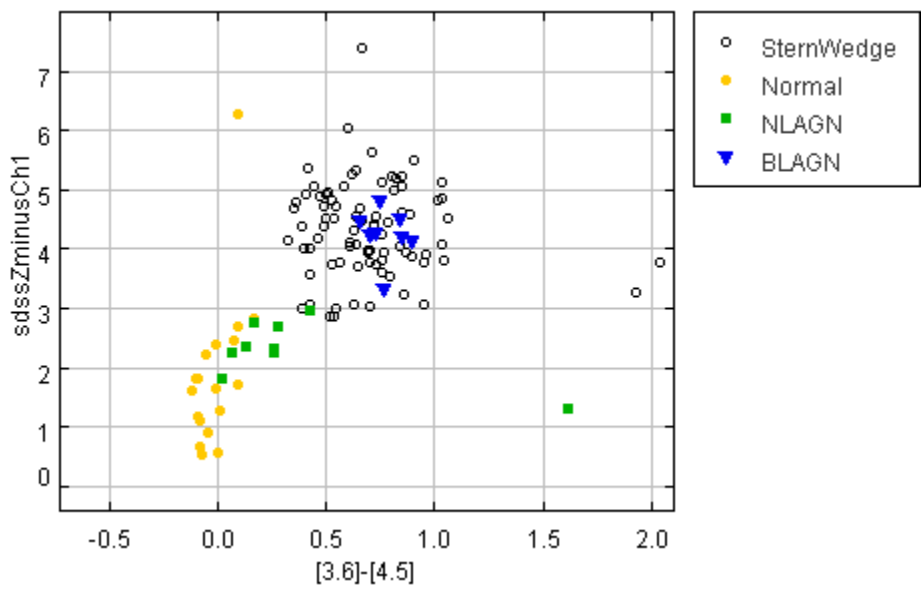

Figure 27: SDSS *z*' - IRAC Color Wedge
Here we have used the color of the longest wavelength SDSS filter with the shortest wavelength IRAC filter.

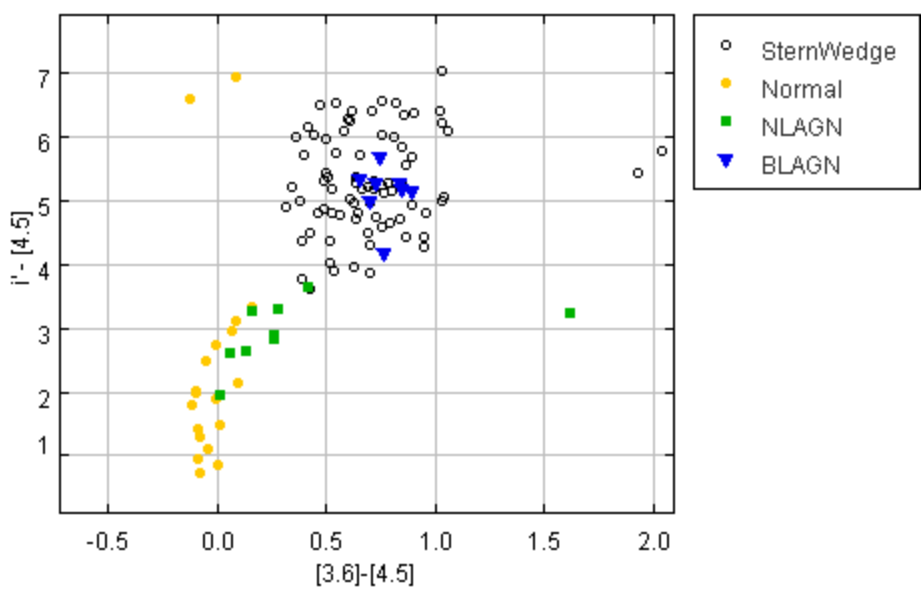

Figure 28: SDSS *i*'-IRAC Color Wedge
Here we have used the color of the *i*' filter and longest wavelength IRAC "warm" mission filter.

E. Candidate Obscured AGN

In the previous sections, we have analyzed and compared various X-ray, mid-infrared, and optical selection techniques comparing to what extent they select sources within our X-ray selected sample. The correspondence between the mid-infrared and optical spectra is a good consistency check on the mid-infrared photometry, since most of these techniques were derived from mid-infrared selected samples correlated with optical spectra. Thus, we have used the mid-infrared techniques to select those X-ray selected sources that meet their criteria. In addition, we have compared the optical/X-ray and infrared/X-ray properties, and found much less correspondence between the parameters. Incorporating both X-ray selection and the optical/infrared criteria, we list in Table 5 a candidate list of hard X-ray (HR > 0) and optical power-law ($-2<\alpha_{opt}<-1$) selected sources.

F. ULX & X-ray Binary Candidates Contaminating the AGN Sample

Ultraluminous X-ray sources (ULXs) and X-ray binaries are both point sources found within various galaxies. ULXs are defined as being bright ($L_X > \sim 10^{39}$ erg/s), point sources found outside the nuclear region of their host galaxy. While the underlying physics for AGN is considered to have the same constituents, a supermassive black hole and active accretion processes, the potential physical scenarios for ULXs remains open to a variety of processes including possible intermediate mass black holes (IMBHs).

Where examining AGN and candidate obscured AGN is the context of this survey, we will mention the level of contamination expected by ULX sources and X-ray binaries. To identify possible contaminating candidates, the X-ray catalog was cross-matched with the Third Reference Catalog of Bright Galaxies (RC3) (de Vaucouleurs et al., 1991). All sources located within a distance equal to the D_{25} semi-major axis were identified and luminosities were calculated assuming the redshift of the RC3 host galaxy. Within fields containing RC3 galaxies, 25% (1341/5297) of the X-ray sources are found to be located within a distance less than the D_{25} semi-major axis and 3 arcseconds outside the nucleus. Assuming each of these sources to be at the distance of the RC3 galaxy, 160 sources have $L_X > 10^{39}$ erg/s. In the context of the entire catalog, the contamination rate would be 1.6%. Applying the same criteria that selected the obscured AGN candidates, we find that there are 4 possible X-ray binary contaminants and no ULX source contaminants.

5. X-RAY BACKGROUND

A. X-ray Number Counts

In order to construct the differential log*N*-log*S* relation, we used the effective area curves of Alexander et al. (2003) and the effective area curve based on our survey, Figure 30. To account for flux-dependent effective area for each observation, we utilized the limiting sensitivity maps included in the Chandra Point Source Catalog calibration files, such as Figure 29. For a few observations that had missing sensitivity maps, we substituted similar observations having the same chip array, approximately the same exposure length, and nearest time of observation. These maps were based on a 3σ flux significance, so are a conservative estimate to the effective area.

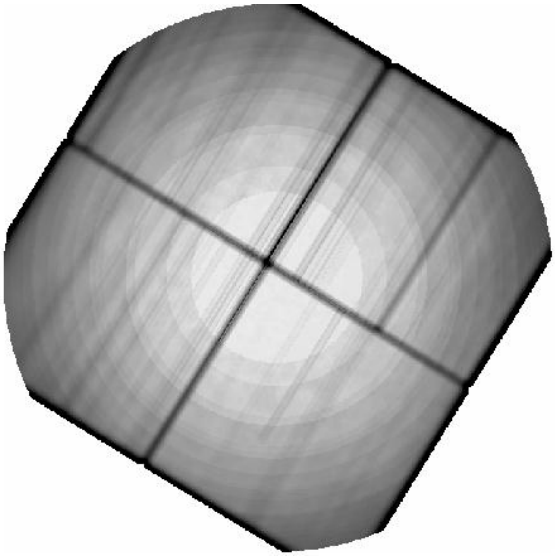

Figure 29: ACIS Observation Sensitivity Map
This figure illustrates the varying sensitivity levels as mapped across the four chip ACIS-I array. The brightness levels per pixel show the level of sensitivity, where brighter pixels show greater sensitivity to faint fluxes. Here the square I-array is inscribed within a 10-arcminute circle, masking the off-axis corner regions.

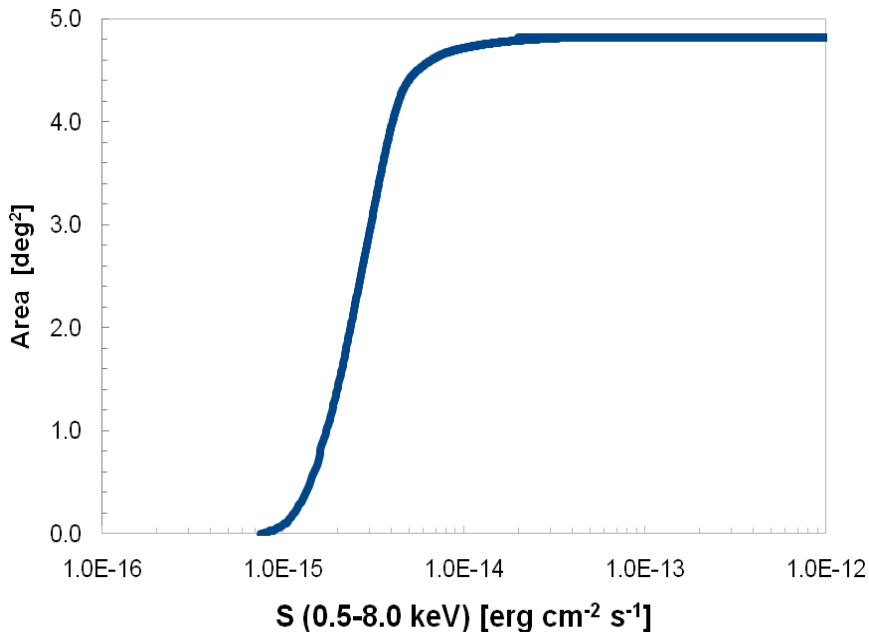

Figure 30: Effective Area Curve
This figure graphs the solid angle versus limiting sensitivity (S/N > 3) for this survey's observations.

In Figure 31, we show the differential log*N*-log*S* relationship for the combination of our survey and the Chandra Deep Fields. By combining the results of the deep fields with our medium-depth wide area survey we are able to better account for intermediate to bright fluxes. The relation was formed similar to Harrison, Eckart, Mao, Helfand, & Stern (2003) by summing over the number of sources within binned flux ranges and weighting by the respective areas of each flux bin:

$$N(>S) = \sum_{S_i > S} \frac{1}{\Omega_i} n(S) = \sum_{S_{j\min}}^{S_{j\max}} \frac{N(S_j)}{\Delta S\ A}, \qquad 8$$

where *n(S)* represents the source surface density within flux bins ΔS, and solid angle *A* that is specified for each source from the effective area curves.

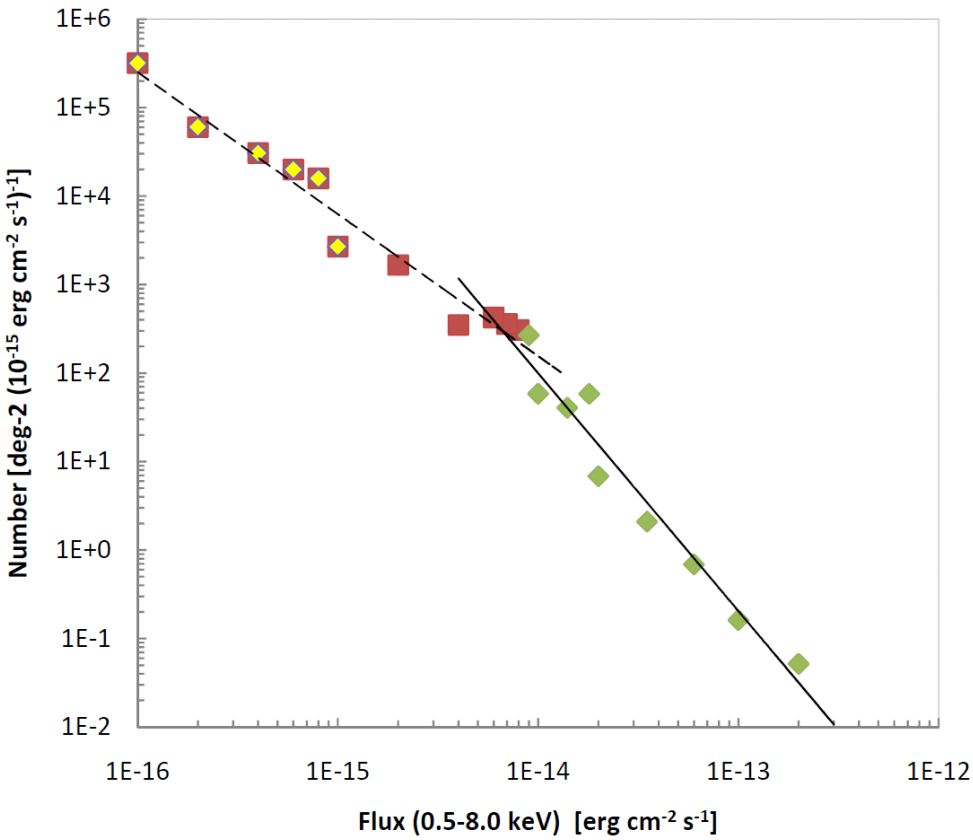

Figure 31: log*N*-log*S* distribution
This figure graphs the number density of sources versus X-ray flux. The green diamonds represent the bright-end sources, the red squares represent the faint sources, and the yellow diamonds represent source bins containing CDF sources.

As can be seen from Figure 31 the data cannot be fit by a single power law, but instead is well fit by two power laws (a broken power-law). The break flux is in the range from S_b = 7-9×10^{-15} ergs cm^{-2} s^{-1}. The faint and bright ends were fit with power-law curves parameterized according to:

$$N(>S) = \sum_{S_i>S} \frac{1}{\Omega_i} n(S) = K(S/10^{-14})^{-\gamma}, \qquad 9$$

where γ is the best-fit slope and *K* is the normalization. For the bright-end (S > 8×10^{-15} ergs cm^{-2} s^{-1}), γ = 2.69±0.25 (within errors of the expectation from an Euclidean distribution) and for the faint-end γ = 1.60±0.05 (significantly deviated from Euclidean). Comparing these slopes with

those of other surveys, we find reasonable agreement: SEXSI (S_b = 1 ×10^{-14}, 1.41±0.17, 2.46±0.08) (Harrison et al., 2003); XMM-2dF (S_b = 6×10^{-14}, 1.8±0.2, 2.3±0.1) (Basilakos et al., 2005); ChaMP (S_b = 1.92 ×10^{-14}, 1.64±0.01, 2.48±0.05) (Kim et al., 2007).

B. Unresolved and Resolved XRB Fractions

As previously mentioned, Figure 1 illustrates the broad spectrum of the XRB, where the data from various past missions are shown. In the energy range of our sample (<10 keV), which is on the rising side of the 30 keV peak, the X-ray Background can be described by a power-law with photon-index of Γ=1.47± 0.06 (Moretti et al., 2009). However, the normalization of the XRB has a large uncertainty. Moretti et al (2009) compiled a short list of measurements from a variety of instruments, listed here including their work with Swift-BAT: (ordered by increasing normalizations): RXTE-PCA, HEAO1, ASCA-SIS, ASCA-GIS, Swift-BAT, Chandra, XMM-Newton, and SAX-MECS. The uncertainties differ by ~30% over a range (in the 2.0-8.0 keV band) from 1.32×10^{-11} ergs cm^{-2} s^{-1} deg^{-2} by Gruber et al. (1999) using HEAO1, to 1.88×10^{-11} ergs cm^{-2} s^{-1} deg^{-2} by Vecchi et al. (1999) using SAX-MECS. Interestingly, though the upper and lower figures are well outside their error bounds, neighboring values in this sequence are within error agreement. Yet as Moretti et al (2009) commented, the discrepancies cannot be explained by a simple difference in absolute calibrations of each instrument (see their section 8 for cross-calibration data checks using simultaneous observations).

For our survey, we performed an internal normalization to the XRB as sampled by our *Chandra* observations. Following the results of our detection probability analysis in Section 2.B.iii, we included only the inner 6 arcminute regions in order to reduce the number of missed faint-sources at greater off-axis angles. In addition, 10 observations were excluded based on their

count rates being greater than 1σ from the sample mean, owing to extended X-ray structures such as hot gas within galaxy clusters. This provided > 2 deg^2 of coverage to be analyzed for the internal XRB normalization.

To account for the instrumental background, we used the *Chandra* stowed-background calibration files matched for exposure length to each observation. Within the area, for each observation, we excluded all observed source counts in regions around each detected source, where the same regions were excluded from the stowed-background files. To more fully exclude source photons from the wings of the PSF, we followed a similar prescription as described by Hickox & Markevitch (2006), where the ~90% encircled energy radius was increased by a factor dependent on the total source counts. Following this scheme, both the total source-free observation counts and the total source-free area of the background region were obtained for each observation. The extraction regions were also reversed to extract each observation's total counts within the source regions.

Using the best fit power-law model, applied by Moretti et al. (2009), to the XRB, we calculated the overall fluxes and intensities derived from our counts and areas. The unresolved background flux for the 0.5-8.0 keV range was 3.44×10^{-12} ergs cm^{-2} s^{-1} and the resolved flux was 2.23×10^{-12} ergs cm^{-2} s^{-1}. Taking into account the areas covered by the background and source regions, the unresolved intensity was 1.68×10^{-12} ergs cm^{-2} s^{-1} deg^{-2} and the resolved intensity was 1.62×10^{-11} ergs cm^{-2} s^{-1} deg^{-2}. The total area covered by the background was 2.05 deg^2, while the source region areas accounted for 0.138 deg^2. Thus, using the total of the unresolved and resolved intensities the fraction left unresolved is 9.4%. Thus, our medium-depth, wide-area

sample resolved XRB fractions of ~ 90% based on our internal measure for the XRB normalization, which was nearer to the normalization found by HEAO-1.

As an alternate measure of the intensity resolved, we used our log*N*-log*S* to integrate the expected resolved intensity. Using the two-power law fit, we integrated the total resolved intensity over the relevant ranges: [3.3×10^{-16}, 8.0×10^{-15}] for the faint-end and [8.0×10^{-15}, 1.0×10^{-11}] for the bright end. The lower-bound flux corresponds to a source having 5 total counts in our deepest observation (162 ks on ACIS-I). This integration yielded a value of 1.58×10^{-11} ergs cm^{-2} s^{-1} deg^{-2} (in the 0.5-8.0keV band), very similar to our internal resolved intensity.

i. Estimation to the X-ray Background Peak

The peak of the XRB (~30 keV) is well beyond the energy range Chandra's imaging X-ray instruments, so no chance at this time of using *Chandra*'s superb spatial resolution to find sources within the peak energy range. However, based on our current sample results, best fit XRB spectral models by Moretti et al. (2009), and insights from synthesis models such as Gilli et al. (2007), we estimated some boundary parameters for AGN contribution. For example, we considered only a single population model constrained by our total resolved 0.5-8.0 keV flux. Here, we neglected any contribution from absorbed AGN, and ascribed all of the 0.5-8.0keV flux to unabsorbed AGN (modeled using a cut-off powerlaw with exponential energy roll-off at ~100 keV and $\Gamma = 1.7$). This provided an upper limit on unabsorbed AGN contribution, which underestimated the peak of the XRB by greater than 30% from what is needed in the10-40 keV range. We then used a two population model, including unabsorbed and absorbed ($N_H = 10^{22}$ cm^{-2}) AGN, constrained by our resolved flux for sources having HR>0 (3.85×10^{-12} ergs cm^{-2} s^{-1}), and found a better approximation to the flux of the XRB peak, but still an underestimate by 20%. Finally, we used a four population model, where we considered an unabsorbed AGN, a mildly

absorbed AGN ($N_H = 10^{21}$ cm^{-2}), and two increasingly absorbed AGN ($N_H = 10^{22}$ cm^{-2}; $N_H = 10^{23}$ cm^{-2}). We followed a similar breakdown as discussed in Gilli et al. (2007), where the flux contribution ratio for mildly absorbed to unabsorbed is ~1:1 and the flux contribution ratio between absorbed sub-groups was ~3:1 (favoring the more heavily absorbed population). Here the two broad groups were constrained by our resolved flux. For this model, the XRB peak (10-40 keV) flux was matched almost entirely. This final model provides a more heavily absorbed population that contributes very little to the current resolved energy range, but could include contributions from Compton-thick AGN that are outside the reach of the 10keV upper limit on *Chandra*'s ACIS detector. The resolved fractions and estimates of unabsorbed AGN, puts tight constraints on any missing population of unabsorbed AGN and on mildly absorbed AGN, as their numbers could not be substantially higher as constrained by the XRB. The absorbed AGN in the range from 10^{22} to 10^{23} cm^{-2} place the best present constraints on the probable populations of Compton-thick AGN.

Several previous studies (Bauer et al, 2004; Worsley et al, 2005), discussed the correction needed for bright sources when analyzing resolved fractions of the XRB from the deep fields, Chandra Deep Field-North (CDF-N), -South (CDF-S) and the Lockman Hole. Worsley et al (2005) made their upper flux-cut at 5×10^{-14} ergs cm^{-2} s^{-1} (removing ~10 sources from CDFs). The advantage of a medium-depth, wide-area sample is that our sample did not suffer from low-number statistics when it came to the bright sources; instead we had ~170 sources above the Worsley cut. Moretti et al (2003) discussed bright sources ~8×10^{-12} to 10^{-11} could account for ~3% in the soft and ~2% in the hard. Making upper-bound flux cuts to our sample, we find sources above ~10^{-13} account for just over 1% in the soft and less than 1% in the hard.

6. CONCLUSION

A. Summary

In the era of the Chandra X-ray Observatory, it has been shown that the cosmic X-ray background can be resolved efficiently into discrete sources, where the sources are dominated by AGN. Using the sample criteria defined in this project, we selected 90 moderate-depth observations (> 60ks) that would enable a survey for serendipitously observed background AGN. From the analysis of the X-ray data, we have identified 10,207 X-ray selected AGN candidates within a FOV of 5.6 deg^2 and to a flux-limit of 9.30×10^{-16}. For these sources, we have cataloged their positions, counts, fluxes (multiple bands), Hardness Ratios (HR), column density (N_H, either from direct spectral fitting or through HR-estimations), and photon indices (for spectral quality sources).

Using the HR technique to distinguish hard-source candidates, we identified 2231 sources with an HR > 0. Of the sources with HR > 0, 126 were found to have an $N_H > 10^{22}$ cm^{-2} (the criteria for obscured AGN) with all being determined by direct spectral fitting (109 with fixed photon index of $\Gamma = 1.7$, or 17 with both N_H and Γ as free parameters). For comparison, only 17 sources with HR < 0 had $N_H > 10^{22}$.

We tested various mid-infrared AGN selection techniques, including infrared power-laws and the color-space "wedge" criteria of Lacy et al. (2004) and Stern et al. (2005), in order to compare the multiwavelength properties of our large X-ray selected sample. Previous IR studies by Lacy et al. (2004) and Stern et al. (2005) used the mid-infrared capabilities of Spitzer, in

accord with optical spectroscopy, to develop photometric constraints by which to sub-divide their IR-selected samples, mainly into broad-line AGN (typical type-1s) and non-broadline galaxies (possible hosts for type-2 AGN). Thus we performed the same photometric criteria on our X-ray selected sample to test if there could be any analogous separation seen in the X-ray properties. Although the spectrally classified sources fell into the correct regions defined in the color-color diagrams, there was no significant correlation with X-ray hardness and by extension X-ray obscuration. We did find where the mid-infrared selection techniques showed an anti-correlation between the rate of selection and X-ray flux for the broad-line AGN. The criteria by Lacy selected a greater proportion of the X-ray sources, despite sampling a smaller color-space wedge than the Stern criteria, thus more restrictive in selecting the X-ray AGN candidates.

Since the "wedge" techniques were designed to select BLAGN, solely IRAC based selection criteria may miss significant numbers of low-luminosity or obscured AGN that are host-dominated (i.e., falling in the Normal or NLAGN regions). Thus, to better account for AGN populations these mid-infrared selection techniques should be complemented by some X-ray selection criteria.

Additionally, using the power-law techniques in the mid-infrared and optical we found very good correspondence to the spectral classifications, as well as providing a better connection to the X-ray parameters. In the mid-infrared power-law space, we found what appears to be a possible third population, a seemingly red-straggler group. The interesting nature of this last group is that several previous studies (Alonso-Herrero et al., 2006; Rigby et al., 2005; Stickel et al., 1996) have seen steep optical-IR slopes out to only -2.8, which they discussed as a probable limit for AGN SEDs. Here we have found a small population that could extend this limit. In the

combination of optical and infrared power-law spaces, we found a possible boundary region between the classified BLAGN and both NLAGN and Normal. This region could be the host to obscured AGN candidates, for which we have listed those candidates that satisfy both the optical criteria for this region and have hard X-ray HR values.

Finally, coming back around to the X-ray background and the level of its resolved spectrum, we found that we can resolve nearly all of the XRB in the soft-band (0.5-2.0 keV), and that the resolved fraction in the hard-band is less than 75%. The remaining unresolved fractions do not come from the bright rare sources missed by the pencil-beam deep fields, but instead is due to the elusive hard sources at levels fainter than the deep fields probe.

B. Concluding Remarks

Although this project seeks to address longstanding issues between XRB resolution and the break between AGN selected in X-rays and lower energy regimes, it comes at a critical juncture in its development. Several upcoming, X-ray missions have been given high priority with launches scheduled within 2 to 10 years, including ASTROSAT by the Indian Space Research Organization, eROSITA (extended Roentgen Survey with an Imaging Telescope Array) by collaboration of German and Russian institutions, and the International X-ray Observatory (IXO) by a merger of the Constellation-X program of NASA and the XEUS project of the ESA. These missions will seek out the rather elusive properties of black holes. To be able to properly probe the extent of the observable universe for these massive and supermassive black holes, it is important that we understand the dominating host source for them—AGN. By having a grasp of the distinguishing characteristics, relative abundances (as functions of both luminosity and

spatial distribution), and high-energy spectral contributions, we will be able to more efficiently probe the Cosmos.

REFERENCES

Alexander, D.M., Bauer, F.E., Brandt, W.N., Schneider, D.P., Hornschemeier, A.E., Vignali, C., et al. (2003) The Chandra Deep Field North Survey XIII: 2Ms Point-Source Catalogs. *The Astronomical Journal, 126*, 539-574.

Alonso-Herrero, A., Perez-Gonzalez, P.G., Alexander, D.M., Rieke, G.H., Rigopoulou, D., Le Floc'h, E., et al. (2006) Infrared power-law galaxies in the Chandra Deep Field-South: Active galactic nuclei and ultraluminous infrared galaxies. *The Astrophysical Journal, 640*, 167-184.

Antonucci, R. (1993). Unified models for active galactic nuclei and quasars. *Annual Review of Astronomy & Astrophysics, 31*(1), 473-521.

Baldi, A., Molendi, S., Comastri, A., Fiore, F., Matt, G., & Vignali, C. (2002). The HELLAS2XMM survey I: the X-ray data and the log*N*-log*S* relation. *The Astrophysical Journal, 564*, 190-195.

Ballantyne, D. R., Shi, Y., Rieke, G. H., Donley, J. L., Papovich, C., & Rigby, J. R. (2006). Does the AGN unified model evolve with redshift? Using the X-ray background to predict the mid-infrared emission of AGNs. *The Astrophysical Journal, 653*, 1070-1088.

Barmby, P., Alonso-Herrero, A., Donley, J. L., Egami, E., Fazio, G. G., Georgakakis, A., et al. (2006). Mid-infrared properties of X-ray sources in the Extended Groth strip. *The Astrophysical Journal, 642*, 126-139.

Bauer, F.E., Alexander, D.M., Brandt, W.N., Schneider, D.P., Treister, E., Hornschemeier, A. E., et al. (2004). The Fall of Active Galactic Nuclei and the Rise of Star-forming Galaxies: A Close Look at the Chandra Deep Field X-Ray Number Counts. *The Astronomical Journal, 128*, 2048-2065.

Brandt, W. N., & Hasinger, G. (2005). Deep extragalactic X-ray surveys. *Annual Review of Astronomy & Astrophysics, 43*(1), 827-859.

Brusa, M., Zamorani, G., Comastri, A., Hasinger, G., Cappelluti, N., Civano, F., et al., (2007) The XMM-Newton wide-field survey in the COSMOS field: III. optical identification and multiwavelength properties of a large sample of X-ray selected sources. *The Astrophysical Journal Supplement Series. 172*, 353-367.

Brusa, M., Civano, F., Comastri, A., Miyaji, T., Salvato, M., Zamorani, G., et al. (2010) The XMM-Newton Wide-field Survey in the Cosmos Field (XMM-COSMOS): Demography and Multiwavelength Properties of Obscured and Unobscured Luminous Active Galactic Nuclei. *The Astrophysical Journal. 716,*348-369.

Caccianiga, A., Severgnini, P., Braito, V., Della Ceca, R., Maccacaro, T., Wolter, A., et al. (2004). The XMM-Newton HBS28 sample: Studying the obscuration in hard X-ray selected AGNs. *Astronomy and Astrophysics, 416*, 901-915.

Chandra Proposers' Observatory Guide (version 12.0). (2009).Cambridge, MA:Chandra X-ray Center.

Comastri, A. & Brusa, M. (2008). Extragalactic X-ray surveys: AGN physics and evolution. *Astronomische Nachrichten, 329*, 122.

Comastri, A., Mignoli, M., Ciliegi, P., Severgnini, P. Maiolino, R., Brusa, M., et al. (2002).The HELLAS2XMM Survey II: Multiwavelength observations of P3: An X-ray-bright, optically inactive galaxy. *The Astrophysical Journal, 571*, 771-778.

Comastri, A., Fiore, F., Vignali, C., Matt, G., Perola, G. C., & La Franca, F. (2001). The BeppoSAX High Energy Large Area Survey (HELLAS) III: Testing synthesis models for the X-ray background. *Monthly Notices of the Royal Astronomical Society, 327*(3), 781-787.

Comastri, A., Setti, G., Zamorani, G., & Hasinger, G. (1995). The contribution of AGNs to the X-ray background. *Astronomy and Astrophysics, 296*, 1.

Cowie, L. L., Garmire, G. P., Bautz, M. W., Barger, A. J., Brandt, W. N., & Hornschemeier, A. E. (2002). The 2-8 keV X-ray number counts determined from Chandra blank field observations. *The Astrophysical Journal, 566*, L5-L8.

Cowsik, R., & Kobetich, E. J. (1972). Comment on inverse compton models for the isotropic X-ray back-ground and possible thermal emission from a hot intergalactic gas. *The Astrophysical Journal, 177*, 585.

de Grijp, M. H. K., Miley, G. K., Lub, J., & de Jong, T. (1985). Infrared seyferts: a new population of active galaxies? *Nature, 314*, 240-242.

Dickey, John M., & Lockman, Felix J. (1990). HI in the galaxy. *Annual Review of Astronomy and Astrophysics, 28*, 215-261.

Eckart, M. E., McGreer, I.D., Stern, D., Harrison, F.A., & Helfand, D.J. (2010). A Comparison of X-ray and Mid-Infrared Selection of Obscured Active Galactic Nuclei. *The Astrophysical Journal, 708*, 584-597.

Fabian, A.C & Barcons X. (1992). The origin of the X-ray background. *Annual Review of Astronomy and Astrophysics,30,* 429-456.

Field, G. B., & Perrenod S. C. (1977). Constraints on a dense hot intergalactic medium. *The Astrophysical Journal, 215*, 717-722.

Fiore, F., Brusa, M., Cocchia, F., Baldi, A., Carangelo, N., Ciliegi, P., et al. (2003). The HELLAS2XMM survey. IV. Optical identifications and the evolution of the accretion luminosity in the Universe. *Astronomy and Astrophysics, 409*, 79-90

Freeman, P. E., Kashyap, V., Rosner, R., & Lamb, D. Q. (2002). A wavelet-based algorithm for the spatial analysis of poisson data. *The Astrophysical Journal Supplement Series, 138*, 185-218.

Giacconi, R., Gursky, H., Paolini, F. R., & Rossi, B. B. (1962). Evidence for X-rays from sources outside the Solar System. *Physical Review Letters, 9*, 439-443.

Gilli, R., Salvati, M., & Hasinger, G. (2001). Testing current synthesis models of the X-ray background. *Astronomy and Astrophysics, 366*, 407-417.

Gilli, R., Comastri, A., & Hasinger, G. (2007). The synthesis of the cosmic X-ray background in the Chandra and XMM-Newton era. *Astronomy and Astrophysics, 463*, 79-96.

Green, P. J., Silverman, J. D., Cameron, R. A., Kim, D.-W., Wilkes, B. J., Barkhouse, W. A., et al. (2004). The Chandra multiwavelength project: Optical follow-up of serendipitous Chandra sources. *The Astrophysical Journal Supplement Series, 150*, 43-71.

Gruber, D. E., Matteson, J. L., Peterson, L. E., & Jung, G. V. (1999). The Spectrum of Diffuse Cosmic Hard X-Rays Measured with HEAO 1. *The Astrophysical Journal, 520*, 124-129.

Hao, H., Elvis, M., Civano, F., Lanzuisi, G., Brusa, M., Lusso, E., et al. (2010) Hot-Dust-Poor Type 1 AGNs in the COSMOS Survey. *The Astrophysical Journal, 724*, L59.

Harrison, F. A., Eckart, M. E., Mao, P. H., Helfand, D. J., & Stern, D. (2003). The serendipitous extragalactic X-ray source identification program I: Characteristics of the hard X-ray sample. *The Astrophysical Journal, 596*, 944-956.

Kim, D.-W., Cameron, R. A., Drake, J. J., Evans, N. R., Freeman, P., Gaetz, T. J., et al. (2004). Chandra multiwavelength project I: First X-ray source catalog. *The Astrophysical Journal Supplement Series, 150*, 19-41.

Lacy, M., Storrie-Lombardi, L. J., Sajina, A., Appleton, P. N., Armus, L., Chapman, S. C., et al. (2004). Obscured and unobscured active galactic nuclei in the Spitzer space telescope first look survey. *The Astrophysical Journal Supplement Series, 154*, 166-169.

Leipski, C., Haas, M., Meusinger, H., Siebenmorgen, R., Chini, R., Scheyda, C. M., et al. (2005). The ISO-2MASS AGN survey: on the type-1 sources. *Astronomy and Astrophysics, 440*, L5-L8.

Lutz, D., Maiolino, R., Spoon, H. W. W., & Moorwood, A. F. M. (2004). The relation between AGN hard X-ray emission and mid-infrared continuum from ISO spectra: Scatter and unification aspects. *Astronomy and Astrophysics, 418*, 465-473.

Maccacaro, T., Gioia, I. M., Wolter, A., Zamorani, G., & Stocke, J. T. (1988). The X-ray spectra of the extragalactic sources in the Einstein Extended Medium Sensitivity Survey. *The Astrophysical Journal, 326*, 680-690.

Manners, J. C., Johnson, O., Almaini, O., Willott, C. J., Gonzalez-Solares, E., Lawrence, A., et al. (2003) The ELAIS deep X-ray survey I: Chandra source catalogue and first results. *Monthly Notices of the Royal Astronomical Society, 343*, 293-305.

Marshall, F. E., Boldt, E. A., Holt, S. S., Miller, R. B., Mushotzky, R. F., Rose, L. A., et al. (1980). The diffuse X-ray background spectrum from 3 to 50 keV. *The Astrophysical Journal, 235*, 4-10.

Moretti, A., Campana, S., Lazzati, D., & Tagliaferri, G. (2003). The Resolved Fraction of the Cosmic X-ray Background. *The Astrophysical Journal, 588*, 696-703.

Moretti, A., Pagani, C., Cusumano, G., Campana, S., Perri, M., Abbey, A., et al. (2009). A new measurement of the cosmic X-ray background. *Astronomy and Astrophysics, 493*, 501-509.

Mushotsky, R.F. (1984). X-ray spectra and time variability of active galactic nuclei. *Advances in Space Research, 3*, 157-165.

Nenkova, M., Sirocky, M. M., Nikutta, R., Ivezić, Ž., & Elitzur, M. (2008). AGN Dusty Tori II. Observational Implications of Clumpiness. *The Astrophysical Journal, 685*, 160-180.

Polletta, M., Wilkes, B., Siana, B., Lonsdale, C., Kilgard, R., Smith, H., et al. (2006). Chandra and Spitzer unveil heavily obscured Quasars in the Chandra/SWIRE survey. *The Astrophysical Journal, 642*, 673-693.

Polletta, M., Tajer, M., Maraschi, T., Trinchieri G., Lonsdale C.J., Chiappetti, L., et al. (2007). Spectral Energy Distributions of Hard X-ray Selected Active Galactic Nuclei in the XMM-Newton Medium Deep Survey. *The Astrophysical Journal, 663*, 81-102.

Rigby, J.R., Rieke, G.H., Pérez-González, P.G., Donley, J.L., Alonso-Herrero, A., Huang, J.-S., et al. (2005). Why Optically Faint AGNs Are Optically Faint: The Spitzer Perspective. *The Astrophysical Journal, 627*, 134-139.

Rigby, J. R., Rieke, G. H., Maiolino, R., Gilli, R., Papovich, C., Pérez-González, P. G., et al. (2004). 24 micron properties of X-ray-selected active galactic nuclei. *The Astrophysical Journal Supplement Series, 154*, 160-165.

Schmitt, J. H. M. M., Snowden, S. L., Aschenbach, B., Hasinger, G., Pfeffermann, E., Predehl, P., et al. (1991). A soft X-ray image of the moon. *Nature, 349*, 583-587.

Spitzer Observer's Manual (version 7.1). (2006). Pasadena, CA:Jet Propulsion Laboratory.

Steidel, C.C., Hunt, M.P., Shapley, A.E., Adelberger, K.L., Pettini, M., Dickinson, M., et al. (2002). The population of faint optically selected active galactic nuclei at z ~ 3. *The Astrophysical Journal, 576*, 653-659.

Stern, D., Eisenhardt, P., Gorjian, V., Kochanek, C. S., Caldwell, N., Eisenstein, D., et al. (2005). Mid-infrared selection of active galaxies. *The Astrophysical Journal, 631*, 163-168.

Stickel, M., Rieke, G.H., Kuehr, H., & Rieke, M.J. (1996). Flat-Spectrum Radio Sources with Faint Optical Counterparts. *The Astrophysical Journal, 468*, 556.

Treister, E., & Urry, C. M. (2005). Active galactic nuclei unification and the X-ray background. *The Astrophysical Journal, 630*, 115-121.

Treister, E., Castander, F. J., Maccarone, T. J., Gawiser, E., Coppi, P. S., Urry, C. M., et al. (2005). The Calán-Yale deep extragalactic research (CYDER) survey: Optical properties and deep spectroscopy of serendipitous X-ray sources. *The Astrophysical Journal, 621*, 104-122.

Treister, E., Urry, C. M., Chatzichristou, E., Bauer, F., Alexander, D. M., Koekemoer, A., et al. (2004). Obscured active galactic nuclei and the X-ray, optical, and far-infrared number counts of active galactic nuclei in the GOODS fields. *The Astrophysical Journal, 616*, 123-135.

Turner, T. J., & Pounds, K. A. (1989). The EXOSAT spectral survey of AGN. *Monthly Notices of the Royal Astronomical Society, 240*, 833-880.

Ueda, Y., Akiyama, M., Ohta, K., Miyaji, T. (2003). Cosmological evolution of the hard X-ray active galactic nucleus luminosity function and the origin of the hard X-ray background. *The Astrophysical Journal, 598*, 886-908.

Vecchi, A., Molendi, S., Guainazzi, M., Fiore, F., & Parmar, A. N. (1999). The BeppoSAX 1-8 keV cosmic background spectrum. *Astronomy and Astrophysics, 349*, L73-L76.

Wang, J. X., Malhotra, S., Rhoads, J. E., Brown, M. J. I., Dey, A., Heckman, T. M., et al. (2004). The 172 ks Chandra exposure of the LALA Bootes field: X-ray source catalog. *The Astronomical Journal, 127*, 213-229.

Worsley, M. A., Fabian, A. C., Bauer, F. E., Alexander, D. M., Hasinger, G., Mateos, S., et al. (2005). The unresolved hard X-ray background: the missing source population implied by the Chandra and XMM-Newton deep fields. *Monthly Notices of the Royal Astronomical Society, 357*, 1281-1287.

Worsley, M. A., Fabian, A. C., Bauer, F. E., Alexander, D. M., Brandt, W. N., & Lehmer, B. D. (2006). Can the unresolved X-ray background be explained by the emission from the optically-detected faint galaxies of the GOODS project? *Monthly Notices of the Royal Astronomical Society, 368*, 1735-1741.

Zier, C. & Biermann, P. L. (2002). Binary black holes and tori in AGN II: Can stellar winds constitute a dusty torus? *Astronomy and Astrophysics, 396*, 91-108.

Table 1: X-ray Energy Bands

Broad:	0.3 - 9.5 keV	Standard Broad:	0.5 – 8.0 keV
Soft:	0.3 - 2.1 keV	Standard Soft:	0.5 – 2.0 keV
Hard:	2.1 - 9.5 keV	Standard Hard:	2.0 – 8.0 keV
		Low Soft:	0.5 – 1.2 keV
		Medium:	1.2 – 2.0 keV

Table 2: X-ray Survey Comparisons

Survey	Observations number	Minimum ksec	Maximum ksec	Average ksec	Total Msec
CYDER[a]	5	30.16	75.15	53.03	0.265
HELLAS2XMM[b]	15	16.80	116.5	39.91	0.599
SEXSI[c]	27	18.00	186.0	61.04	1.648
ChaMP[d]	130	1.35	126.7	28.90	3.757
UA	90	60.10	162.0	81.11	7.300

[a] (Treister et al., 2005); [b] (Baldi et al., 2002); [c] (Harrison, Eckart, Mao, Helfand, & Stern, 2003); [d] (Kim et al., 2004; We note that there is mentioned in the literature an extended ChaMP survey including 392 observations, but there are no publicly available lists to compare.)

Table 3: X-ray Observations

Target Name	RA (J2000)	Dec (J2000)	Obs ID	Exposure (ks)	Instrument	Data Mode
AC114	344.7020	-34.8020	1562	73.5	ACIS-S	FAINT
V 1121+2327	170.2410	23.4450	1660	72.2	ACIS-I	VFAINT
V 1221+4918	185.3520	49.3040	1662	80.1	ACIS-I	VFAINT
PROTO CLUSTER	334.3850	0.2190	1694	78.9	ACIS-S	FAINT
CL 0848.6+4453	132.2330	44.9140	1708	62.2	ACIS-I	VFAINT
LDN 1551	67.8850	18.1300	1866	79.9	ACIS-I	FAINT
CARTWHEEL	9.4170	-33.7160	2019	77.1	ACIS-S	FAINT
NGC 3556	167.8800	55.6740	2025	60.1	ACIS-S	FAINT
NGC 2681	133.3870	51.3140	2060	81.9	ACIS-S	FAINT
NGC 2681	133.3870	51.3140	2061	80.0	ACIS-S	FAINT
NGC 4125	182.0230	65.1750	2071	65.1	ACIS-S	VFAINT
IC 1459	344.2940	-36.4620	2196	60.2	ACIS-S	FAINT
Abell 2125	235.1870	66.2170	2207	82.6	ACIS-I	VFAINT
3C280	194.2380	47.3390	2210	64.3	ACIS-S	VFAINT
RX J1317.4+2911	199.3410	29.1880	2228	112.8	ACIS-I	VFAINT
QSO 1508+5714	227.5120	57.0450	2241	90.1	ACIS-S	FAINT
RX J0910+5422	137.6890	54.3680	2452	66.2	ACIS-I	VFAINT
PC 0025+0447	6.9250	5.0610	2579	67.2	ACIS-S	VFAINT
NGC 4911	195.2340	27.7910	2941	63.7	ACIS-I	VFAINT
APM08279+5255	127.9230	52.7550	2979	90.3	ACIS-S	FAINT
PG 2112+059	318.7190	6.1280	3011	60.2	ACIS-S	FAINT
UM425	170.8360	1.6300	3013	111.6	ACIS-S	VFAINT
NGC 4038/4039	180.4740	-18.8770	3040	69.9	ACIS-S	FAINT
NGC 4038/4039	180.4740	-18.8770	3041	73.9	ACIS-S	FAINT
NGC 4038/4039	180.4740	-18.8770	3042	68.1	ACIS-S	FAINT
NGC 4038/4039	180.4740	-18.8770	3043	68.0	ACIS-S	FAINT
3C294	211.6840	34.1900	3207	123.6	ACIS-S	VFAINT

SC 1120-1202	170.0380	-12.0330	3235	70.1	ACIS-I	VFAINT
RCS1417+5305	214.2490	53.0870	3239	63.7	ACIS-I	VFAINT
MG J0414+0534	63.6570	5.5790	3419	97.9	ACIS-S	VFAINT
3C294	211.6840	34.1900	3445	70.8	ACIS-S	VFAINT
RCS0439.6-2905*	69.9080	-29.0820	3577	77.2	ACIS-S	VFAINT
NGC 4636*	190.7080	2.6880	3926	75.7	ACIS-I	VFAINT
NGC 1427A	55.0440	-35.6270	3949	66.3	ACIS-S	VFAINT
NGC 3631	170.2620	53.1690	3951	90.2	ACIS-S	VFAINT
SDSS 1306+0356 JET	196.5390	3.9450	3966	119.8	ACIS-S	VFAINT
1136-135	174.7950	-13.8460	3973	77.4	ACIS-S	VFAINT
1150+495	178.3520	49.5190	3974	68.5	ACIS-S	VFAINT
NGC 5252	204.5660	4.5420	4054	63.1	ACIS-S	VFAINT
LALA CETUS FIELD	31.1840	-5.0930	4129	162.0	ACIS-I	VFAINT
CLJ1415.1+3612	213.7970	36.2010	4163	90.4	ACIS-I	VFAINT
Fornax Cluster	54.8770	-35.7560	4175	63.7	ACIS-I	VFAINT
MS1455.0+2232	224.3120	22.3420	4192	93.1	ACIS-I	VFAINT
ABELL 2390	328.4030	17.6960	4193	96.3	ACIS-S	VFAINT
MACS1423.8+2404	215.9490	24.0780	4195	117.1	ACIS-S	VFAINT
CLASS B0712+472	109.0210	47.1510	4199	99.0	ACIS-S	VFAINT
ABELL 520*	73.5160	2.8920	4215	67.2	ACIS-I	VFAINT
NGC 4636*	190.7080	2.6880	4415	75.3	ACIS-I	VFAINT
LDN 1448*	51.4020	30.7540	4497	68.8	ACIS-I	VFAINT
Coma Cluster	194.5010	27.3610	4724	60.4	ACIS-I	VFAINT
NGC 4217	183.9620	47.0930	4738	73.7	ACIS-S	FAINT
NGC 4013*	179.6300	43.9470	4739	80.1	ACIS-S	FAINT
NGC 625	23.7780	-41.4370	4746	61.1	ACIS-S	VFAINT
NGC 7714	354.0590	2.1550	4800	60.2	ACIS-S	FAINT
RX J105343+5735*	163.4290	57.5830	4936	93.4	ACIS-S	FAINT
4C+55.16	128.7290	55.5730	4940	97.2	ACIS-S	VFAINT
Centaurus Cluster	192.2040	-41.3120	4954	90.2	ACIS-S	FAINT
RXJ 1159+5531	179.9640	55.5340	4964	76.1	ACIS-S	VFAINT

Hydra A	139.5240	-12.0950	4970	100.1	ACIS-S	VFAINT
Abell 496*	68.4040	-13.2380	4976	76.1	ACIS-S	VFAINT
Abell 2029	227.7340	5.7440	4977	78.9	ACIS-S	FAINT
RCS0224-0002*	36.1420	-0.0420	4987	90.2	ACIS-S	VFAINT
Abell 1413	178.8250	23.4050	5003	76.1	ACIS-I	VFAINT
1E0657-56	104.5830	-55.9420	5356	98.5	ACIS-I	VFAINT
1E0657-56	104.5830	-55.9420	5361	83.7	ACIS-I	VFAINT
HH 154	67.8850	18.1300	5381	98.2	ACIS-I	FAINT
M82	148.9590	69.6800	5644	75.1	ACIS-S	GRADED
H 1413+117	213.9380	11.4950	5645	90.0	ACIS-S	VFAINT
PKS 1127-145	172.5300	-14.8240	5708	116.3	ACIS-S	VFAINT
CL0230+1836	37.6110	18.6060	5754	68.7	ACIS-I	VFAINT
ABELL 4059	359.2530	-34.7590	5785	93.3	ACIS-S	VFAINT
SDSS J1004+4112	151.1420	41.2120	5794	81.1	ACIS-S	VFAINT
Abell 2052	229.1850	7.0210	5807	128.6	ACIS-S	VFAINT
MACS1311.0-0311	197.7570	-3.1770	6110	64.0	ACIS-I	VFAINT
NGC 3801	175.0710	17.7280	6843	60.2	ACIS-S	VFAINT
Abell 1835	210.2590	2.8790	6880	119.5	ACIS-I	VFAINT
Abell 1689	197.8730	-1.3420	6930	77.2	ACIS-I	VFAINT
VV 114	16.9470	-17.5070	7063	60.1	ACIS-S	VFAINT
NGC 3379	161.9570	12.5820	7073	85.2	ACIS-S	FAINT
NGC 3379	161.9570	12.5820	7074	70.0	ACIS-S	VFAINT
NGC 3379*	161.9570	12.5820	7075	84.2	ACIS-S	VFAINT
NGC 4278	185.0280	29.2810	7077	111.7	ACIS-S	VFAINT
NGC 5253	204.9830	-31.6400	7153	69.1	ACIS-S	FAINT
NGC 5253	204.9830	-31.6400	7154	67.5	ACIS-S	FAINT
CL0405-4100	61.3510	-41.0040	7191	70.1	ACIS-I	VFAINT
M87	187.7060	12.3910	7212	66.1	ACIS-I	VFAINT
Abell 1689	197.8730	-1.3420	7289	76.1	ACIS-I	VFAINT
4C19.44	209.2690	19.3170	7302	72.5	ACIS-S	FAINT
Abell 2597	351.3320	-12.1240	7329	60.9	ACIS-S	VFAINT

XMMU J2235.3-2557	338.8360	-25.9620	7367	80.7	ACIS-S	VFAINT

*Subset of observations were used in a pilot study to evaluate methodology and processing pipeline.

Table 4: Mid-Infrared Source Statistics

IRAC Channel	Number	Mean Flux (mJy)	Mean Magnitude
1 (3.6μm)	2648	90.966	16.529
2 (4.5μm)	2807	62.378	16.073
3 (5.8μm)	2417	115.155	15.112
4 (8.0μm)	2550	151.143	14.468

Table 5: Candidate Obscured AGN

RA (deg)	Dec (deg)	OBSID	Redshift	source	α_{opt}	HR	$F_{0.5\text{-}8.0}$ ergs cm^{-2} s^{-1}	$F_{0.5\text{-}2.0}$ ergs cm^{-2} s^{-1}	$F_{2.0\text{-}8.0}$ ergs cm^{-2} s^{-1}
127.85573	52.72879	2979	0.23	phot-z	-1.89	0.07	1.40E-15	5.20E-16	8.77E-16
128.85748	55.68491	4940	0.18	phot-z	-1.98	0.55	9.67E-16	3.59E-16	6.08E-16
132.15690	44.95328	1708	0.57	ned-z	-1.56	0.30	3.19E-15	1.21E-15	1.98E-15
133.32503	51.24788	2061	0.48	phot-z	-1.90	0.57	3.18E-15	1.21E-15	1.97E-15
151.11828	41.19134	5794	0.22	phot-z	-1.76	0.51	1.40E-15	5.46E-16	8.50E-16
163.41044	57.65586	4936	0.33	phot-z	-1.13	0.15	1.02E-15	4.03E-16	6.20E-16
170.15879	53.07810	3951	0.13	phot-z	-1.78	0.03	3.46E-15	1.35E-15	2.11E-15
170.77763	1.65343	3013	0.33	phot-z	-1.95	0.21	5.97E-16	2.22E-16	3.75E-16
170.83550	1.63142	3013			-1.50	0.36	8.99E-16	3.34E-16	5.65E-16
170.88914	1.63758	3013			-1.68	0.69	1.89E-15	7.03E-16	1.19E-15
170.99069	1.58598	3013	0.05	phot-z	-1.82	0.03	4.84E-15	1.80E-15	3.05E-15
175.14956	17.78646	6843			-1.89	0.29	2.62E-15	1.00E-15	1.61E-15
183.92378	47.08343	4738			-1.86	0.86	1.41E-15	5.49E-16	8.62E-16
185.27890	49.21964	1662	0.09	phot-z	-1.00	0.22	1.22E-15	4.74E-16	7.48E-16
185.45114	49.19216	1662	0.22	phot-z	-1.90	0.03	9.95E-15	3.86E-15	6.09E-15
187.58182	12.41204	7212			-1.49	0.29	3.10E-15	1.18E-15	1.92E-15
187.60020	12.31451	7212			-1.36	0.22	4.18E-15	1.59E-15	2.59E-15
187.70746	12.39746	7212			-1.97	0.10	3.21E-15	1.22E-15	1.99E-15
187.71787	12.44684	7212			-1.78	0.00	1.41E-15	5.37E-16	8.74E-16
187.75960	12.41555	7212			-1.74	0.16	2.22E-16	8.44E-17	1.37E-16
195.16721	27.81926	2941	0.28	phot-z	-1.65	0.18	1.54E-16	6.01E-17	9.34E-17
195.37980	27.90669	2941			-1.41	0.02	8.83E-15	3.46E-15	5.37E-15
197.63618	-3.27241	6110			-1.28	0.03	4.46E-15	1.71E-15	2.75E-15
197.74644	-3.34499	6110			-1.52	0.65	1.75E-15	6.73E-16	1.08E-15
197.78001	-1.39648	7289			-1.28	0.75	4.41E-15	1.70E-15	2.71E-15
197.84707	-1.27140	6930			-1.05	0.65	8.06E-16	3.11E-16	4.96E-16

199.15152	29.20294	2228			-1.37	0.21	6.06E-15	2.37E-15	3.69E-15
199.20419	29.03424	2228			-1.45	0.06	7.62E-16	2.97E-16	4.64E-16
199.34201	29.19038	2228	0.18	phot-z	-1.47	0.61	1.99E-15	7.76E-16	1.21E-15
199.42780	29.15353	2228	0.18	phot-z	-1.56	0.86	1.28E-15	4.99E-16	7.78E-16
210.18047	2.86909	6880			-1.53	0.02	1.98E-15	7.57E-16	1.22E-15
210.20359	2.98122	6880			-1.06	0.52	5.51E-15	2.11E-15	3.40E-15
210.38970	2.77892	6880	0.41	phot-z	-1.62	0.79	5.72E-16	2.19E-16	3.53E-16
211.79248	34.32579	3445	0.13	phot-z	-1.48	0.87	2.43E-15	9.48E-16	1.49E-15
211.85711	34.25291	3207	0.38	phot-z	-1.12	0.33	3.13E-15	1.22E-15	1.91E-15
213.71483	36.15906	4163	0.05	phot-z	-1.59	0.87	1.82E-15	7.10E-16	1.11E-15
213.77627	36.02188	4163	0.28	phot-z	-1.42	0.16	2.93E-15	1.14E-15	1.79E-15
213.81994	36.24378	4163	0.25	phot-z	-1.87	0.73	3.74E-15	1.46E-15	2.28E-15
213.87339	36.28003	4163	0.89	phot-z	-1.35	0.35	1.61E-15	6.29E-16	9.84E-16
213.90402	36.11474	4163	0.30	phot-z	-1.63	0.35	4.42E-15	1.73E-15	2.70E-15
213.97769	36.15993	4163	0.06	phot-z	-1.98	0.02	5.79E-16	2.26E-16	3.53E-16
214.02880	53.15834	3239			-1.83	0.17	8.58E-15	3.34E-15	5.24E-15
214.34446	52.98096	3239	0.04	phot-z	-1.75	0.04	6.52E-15	2.53E-15	3.98E-15
214.35953	53.10199	3239	0.31	phot-z	-1.88	0.58	1.82E-15	7.09E-16	1.11E-15
215.97041	24.15045	4195	0.05	phot-z	-1.08	0.47	1.72E-15	6.56E-16	1.07E-15
227.35322	57.18090	2241	0.24	phot-z	-1.39	0.49	9.57E-15	3.71E-15	5.86E-15
227.40525	57.08536	2241	0.44	phot-z	-1.37	0.83	8.48E-16	3.29E-16	5.19E-16
229.22889	7.07264	5807	0.07	phot-z	-1.96	1.00	6.16E-17	2.34E-17	3.83E-17
318.61726	6.25856	3011			-1.62	0.32	4.81E-15	1.71E-15	3.09E-15
334.39801	0.19159	1694			-1.18	0.31	1.62E-15	5.98E-16	1.03E-15
334.41473	0.25774	1694	0.54	ned-z	-1.51	0.06	1.61E-15	5.93E-16	1.02E-15

Table 6: XRB Intensities

	Current	CDF[a]	HEAO-1[b]	SAX-MECS[c]
Total	1.79+0.09	2.51+.20	1.97+0.17	2.80+0.10
Resolved	1.62+0.07	2.01+0.10	--	--
Unresolved	0.168+0.06	0.50+0.17	--	--

Notes: All intensities are converted to the 0.5-8.0keV range, and are in units of 10^{-11} ergs cm^{-2} s^{-1} deg^{-2} .
[a]Hickox & Markevitch (2006); [b]Gruber et al. (1999); [c] Vecchi et al. (1999)